4. Feng JQ, Ward LM, Liu S, Lu Y, Xie Y, Yuan B, Yu X, Rauch F, Davis SI, Zhang S, Rios H, Drezner MK, Quarles LD, Bonewald LF, White KE (2006) Loss of DMP1 causes rickets and osteomalacia and identifies a role for osteocytes in mineral metabolism. Nat Genet 38:1310–1315

5. Fukumoto S, Martin TJ (2009) Bone as an endocrine organ. Trends Endocrinol Metab 20:230–236

6. Shimada T, Kakitani M, Yamazaki Y, Hasegawa H, Takeuchi Y, Fujita T, Fukumoto S, Tomizuka K, Yamashita T (2004) Targeted ablation of Fgf23 demonstrates an essential physiological role of FGF23 in phosphate and vitamin D metabolism. J Clin Invest 113:561–568

7. Razzaque MS (2009) The FGF23-Klotho axis: endocrine regulation of phosphate homeostasis. Nat Rev Endocrinol 5:611–619

8. Toyosawa S, Shintani S, Fujiwara T, Ooshima T, Sato A, Ijuhin N, Komori T (2001) Dentin matrix protein 1 is predominantly expressed in chicken and rat osteocytes but not in osteoblasts. J Bone Miner Res 16:2017–2026

9. Weiss RE, Watabe N (1979) Studies on the biology of fish bone. III. Ultrastructure of osteogenesis and resorption in osteocytic (cellular) and anosteocytic (acellular) bones. Calcif Tissue Int 28:43–56

10. Peignoux-Deville J, Lallier F, Vidal B (1982) Evidence for the presence of osseous tissue in dogfish vertebrae. Cell Tissue Res 222:605–614

11. Ekanayake S, Hall BK (1987) The development of acellularity of the vertebral bone of the Japanese medaka, *Oryzias latipes* (Teleostei; Cyprinidontidae). J Morphol 193:253–261

12. Hughes DR, Bassett JR, Moffat LA (1994) Histological identification of osteocytes in the allegedly acellular bone of the sea breams *Acanthopagrus australis*, *Pagrus auratus* and *Rhabdosargus sarba* (Sparidae, Perciformes, Teleostei). Anat Embryol 190:163–179

13. Witten PE, Huysseune A (2009) A comparative view on mechanisms and functions of skeletal remodelling in teleost fish, with special emphasis on osteoclasts and their function. Biol Rev Camb Philos Soc 84:315–346

14. Miura S, Hanaoka K, Togashi S (2008) Skeletogenesis in *Xenopus tropicalis*: characteristic bone development in an anuran amphibian. Bone 43:901–909

15. Rubinacci A, Villa I, Dondi Benelli F, Borgo E, Ferretti M, Palumbo C, Marotti G (1998) Osteocyte-bone lining cell system at the origin of steady ionic current in damaged amphibian bone. Calcif Tissue Int 63:331–339

16. Anderson MP, Capen CC (1976) Fine structural changes of bone cells in experimental nutritional osteodystrophy of green iguanas. Virchows Arch B Cell Pathol 20:169–184

17. Zimmer C (2007) Evolution. Jurassic genome. Science 315:1358–1359

18. Pyati UJ, Webb AE, Kimelman D (2005) Transgenic zebrafish reveal stage-specific roles for Bmp signaling in ventral and posterior mesoderm development. Development 132:2333–2343

19. Inohaya K, Takano Y, Kudo A (2007) The teleost intervertebral region acts as a growth center of the centrum: in vivo visualization of osteoblasts and their progenitors in transgenic fish. Dev Dyn 236:3031–3046

20. Renn J, Winkler C (2009) Osterix-mCherry transgenic medaka for in vivo imaging of bone formation. Dev Dyn 238:241–248

21. Inohaya K, Takano Y, Kudo A (2010) Production of Wnt4b by floor plate cells is essential for the segmental patterning of the vertebral column in medaka. Development 137:1807–1813

22. Hirose S, Li M, Kojima T, de Freitas PH, Ubaidus S, Oda K, Saito C, Amizuka N (2007) A histological assessment on the distribution of the osteocytic lacunar canalicular system using silver staining. J Bone Miner Metab 25:374–382

23. Moss ML (1961) Studies of the acellular bone of teleost fish. I. Morphological and systematic variations. Acta Anat 46:343–362

24. Moss ML (1962) Studies of the acellular bone of teleost fish. II. Response to fracture under normal and acalcemic conditions. Acta Anat 48:46–60

ORIGINAL ARTICLE

TGF-β drives epithelial-mesenchymal transition through δEF1-mediated downregulation of ESRP

K Horiguchi[1], K Sakamoto[2], D Koinuma[1], K Semba[3], A Inoue[4], S Inoue[4], H Fujii[4], A Yamaguchi[2], K Miyazawa[5], K Miyazono[1] and M Saitoh[1,5]

[1]Department of Molecular Pathology, Graduate School of Medicine, University of Tokyo, Tokyo, Japan; [2]Section of Oral Pathology, Graduate School of Medical and Dental Sciences, Tokyo Medical and Dental University, Tokyo, Japan; [3]Department of Life Science and Medical Bio-Science, Waseda University, Tokyo, Japan; [4]First Department of Surgery, Interdisciplinary Graduate School of Medicine and Engineering, University of Yamanashi, Yamanashi, Japan and [5]Department of Biochemistry, Interdisciplinary Graduate School of Medicine and Engineering, University of Yamanashi, Yamanashi, Japan

Epithelial-mesenchymal transition (EMT) is a crucial event in wound healing, tissue repair and cancer progression in adult tissues. We have recently shown that transforming growth factor (TGF)-β-induced EMT involves isoform switching of fibroblast growth factor receptors by alternative splicing. We performed a microarray-based analysis at single exon level to elucidate changes in splicing variants generated during TGF-β-induced EMT, and found that TGF-β induces broad alteration of splicing patterns by downregulating epithelial splicing regulatory proteins (ESRPs). This was achieved by TGF-β-mediated upregulation of δEF1 family proteins, δEF1 and SIP1. δEF1 and SIP1 each remarkably repressed ESRP2 transcription through binding to the ESRP2 promoter in NMuMG cells. Silencing of both δEF1 and SIP1, but not either alone, abolished the TGF-β-induced ESRP repression. The expression profiles of ESRPs were inversely related to those of δEF1 and SIP in human breast cancer cell lines and primary tumor specimens. Further, over-expression of ESRPs in TGF-β-treated cells resulted in restoration of the epithelial splicing profiles as well as attenuation of certain phenotypes of EMT. Therefore, δEF1 family proteins repress the expression of ESRPs to regulate alternative splicing during TGF-β-induced EMT and the progression of breast cancers.
Oncogene advance online publication, 31 October 2011; doi:10.1038/onc.2011.493

Introduction

Splicing is a post-transcriptional process involved in the maturation of mRNAs and contributes to proteomic diversity by increasing the number of distinct mRNAs generated from a single gene locus. Recent works suggest that more than 90% of human genes can produce different isoforms through alternative splicing (Pan et al., 2008; Wang et al., 2008). This process is tightly regulated in a tissue- and cell-type-dependent fashion (Matlin et al., 2005; Blencowe, 2006), and alterations in this process are often linked to various types of diseases including cancer (Wang and Cooper, 2007; Dutertre et al., 2010). Aberrations of splicing machinery result from mutations in splicing sites or dysfunction of splicing regulatory factors (Licatalosi and Darnell, 2010).

One of the well-known genes that are regulated by tissue-specific alternative splicing is the fibroblast growth factor receptors (FGFRs). Functional FGFRs are encoded by four genes (FGFR1–FGFR4), and the receptors consist of three extracellular immunoglobulin domains (Ig-I, Ig-II and Ig-III), a single transmembrane domain and a cytoplasmic tyrosine kinase domain (Eswarakumar et al., 2005). FGFRs have several isoforms, as exon skipping removes the Ig-I domain. In addition, alternative splicing in the second half of the Ig-III domain in FGFR1-FGFR3 produces the IIIb (FGFR1IIIb-FGFR3IIIb) and IIIc (FGFR1IIIc-FGFR3IIIc) isoforms that have distinct fibroblast growth factor (FGF)-binding specificities and are predominantly expressed in epithelial and mesenchymal cells, respectively. FGF-2 (basic FGF) and FGF-4 bind preferentially to the IIIc isoforms, whereas FGF-7 (keratinocyte growth factor) and FGF-10 bind exclusively to the IIIb isoforms (Coumoul and Deng, 2003; Chaffer et al., 2007). Recently, epithelial splicing regulatory proteins (ESRPs) 1 and 2 were identified as coordinators of the epithelial cell-type-specific splicing program. ESRPs activate the splicing of exon IIIb and silence the splicing of exon IIIc of FGFR2, leading to the expression of proteins with the epithelial patterns of alternative splicing (Warzecha et al., 2009a,b).

Epithelial-mesenchymal transition (EMT) is the differentiation switch directing polarized epithelial cells to trans-differentiate into mesenchymal cells (Thiery et al., 2009). During the process of embryonic development, wound healing and reorganization in adult tissues, epithelial cells have been shown to lose their epithelial polarity and acquire mesenchymal phenotype. Further,

EMT is involved in the process of invasion of tumor cells which also includes the loss of cell–cell interaction (Kalluri and Weinberg, 2009). Thus far, in nearly all cases, EMT appears to be regulated by extracellular matrix components and soluble growth factors or cytokines (Thiery and Sleeman, 2006). Among these factors, transforming growth factor-β (TGF-β) is considered as the key mediator of EMT during physiological processes. It is frequently and abundantly expressed in various tumors and also induces EMT in cancer cells during cancer progression. Recent studies revealed that TGF-β transcriptionally regulates expression of several transcription factors, including the zinc-finger factors Snail and Slug, the two-handed zinc-finger factors of δEF1 family proteins δEF1 and SIP1, the helix-loop-helix factors Twist and E12/E47, and the high motility group protein family HMGA2, which are involved in the induction of EMT particularly through the transcriptional repression of E-cadherin (Moustakas and Heldin, 2007; Miyazono, 2009).

We have recently reported that TGF-β induces isoform switching of FGFRs from IIIb to IIIc by alternative splicing during EMT in NMuMG cells, which results in enhanced EMT with aggressive phenotypes through cooperative action of TGF-β and FGF-2 (Shirakihara et al., 2011). In the present study, we found that TGF-β regulates alternative splicing of numerous genes during EMT. The expression of δEF1 family proteins, δEF1 and SIP1, is increased after TGF-β treatment and subsequently represses the expression of the alternative splicing factor ESRP. Overexpression of ESRP in TGF-β-treated cells inhibits the conversion of alternative splicing pattern of epithelial types into those of mesenchymal types, as well as downregulation of the expression of E-cadherin. Repression of ESRP by δEF1 family proteins is thus, a crucial process during EMT induced by TGF-β and in progression of breast cancers.

Results

Changes in splice variants during TGF-β-induced EMT

We have recently found that TGF-β primes isoform switching of FGFRs by alternative splicing during TGF-β-induced EMT, thereby changing the sensitivities of cells from FGF-7 to FGF-2 (Shirakihara et al., 2011). Reverse transcriptase-polymerase chain reaction (RT–PCR) analysis of mouse mammary epithelial NMuMG cells revealed that, in addition to FGFRs, CD44 splicing profile and the total level of CD44 mRNA were changed after treatment with TGF-β (Figures 1a and b). There are multiple splice variants of the Mena gene (a member of Enabled (Ena)/vasodilator-stimulated phosphoprotein family of proteins) that are involved in cancer progression (Philippar et al., 2008). We found that TGF-β also caused changes in splicing of the exon 11a of the Mena gene (Figure 1c). These findings suggest that alteration in splicing variants by TGF-β is not limited to FGFRs.

We next analyzed the expression of more than one million exons in NMuMG cells using mouse exon 1.0 ST

array and adapted ARH method to rank the splicing predictions across the different genes (Figure 1d) (Rasche and Herwig, 2010). We found that the expression of 3601 genes was altered at the exon level, which was classified by GO parameters (Lee et al., 2008), suggesting that TGF-β induces a broad alteration in splicing patterns and generates a number of splicing variants during EMT in NMuMG cells (Supplementary Figure S1 and Supplementary Table 1). As CD44, FGFRs, SLK (ste 20-like kinase) and CTNND1 (also known as δ-catenin or p120 catenin), of which splicing profiles have been reported to be regulated by ESRPs, were included in our exon-array data (Figure 1e and Supplementary Figure S2), we calculated ARH scores for the published exon-array data of ESRPs-silenced human prostate cancer PNT2 cells and compared the data with our exon-array data (Warzecha et al., 2009b). We found that 227 genes and 75 genes in ESRP1/2-silenced cells overlapped with those of our data with $P < 0.05$ and $P < 0.01$, respectively (Supplementary Table 2). These findings suggest that TGF-β-induced changes in splice variants are partly mediated by ESRPs.

Repression of ESRPs by TGF-β

We next determined how TGF-β regulates the functions of splicing factors ESRP1 and ESRP2 during EMT. We found that TGF-β considerably downregulated the mRNA expression of ESRP2 in NMuMG cells, whereas the expression of ESRP1 mRNA could not be clearly detected (Figure 2a, left). We also examined the expression of ESRPs after TGF-β stimulation in other cells derived from mammary gland epithelial cells, including EpH4 cells expressing the viral H-Ras oncogene (EpRas cells) and breast cancer JygMC(A) cells (Ehata et al., 2007). Treatment of EpRas cells with TGF-β repressed both ESRP1 and ESRP2 at the mRNA levels and ESRP1 at the protein level (Figures 2a, right and b). As JygMC(A) cells autonomously secrete TGF-β (Hoshino et al., 2011), we treated the cells with TGF-β type I receptor (TβR-I) inhibitor, SB431542. The treatment increased the expression of ESRP1 and ESRP2 (Figure 2c). In addition, transfection of NMuMG cells with small interfering RNAs (siRNAs) against Smad2 and Smad3 attenuated the effects of TGF-β on the expression of ESRP2 (Figure 2d). Moreover, when de novo protein synthesis was inhibited by cycloheximide, which is an inhibitor of protein synthesis, downregulation of ESRP2 by TGF-β was attenuated (Figure 2e). PAI-1 and SIP1 have been reported as direct and indirect transcriptional targets of TGF-β/Smad pathway, respectively (Shirakihara et al., 2007). Thus, these findings suggest that the suppression of ESRP2 by TGF-β involves de novo protein synthesis through the Smad pathway.

ESRP2 repression by δEF1 and SIP1 in TGF-β-induced EMT

We examined the expression profiles of δEF1, SIP1, E-cadherin and ESRP2 after TGF-β stimulation by quantitative RT–PCR. The levels of ESRP2 were
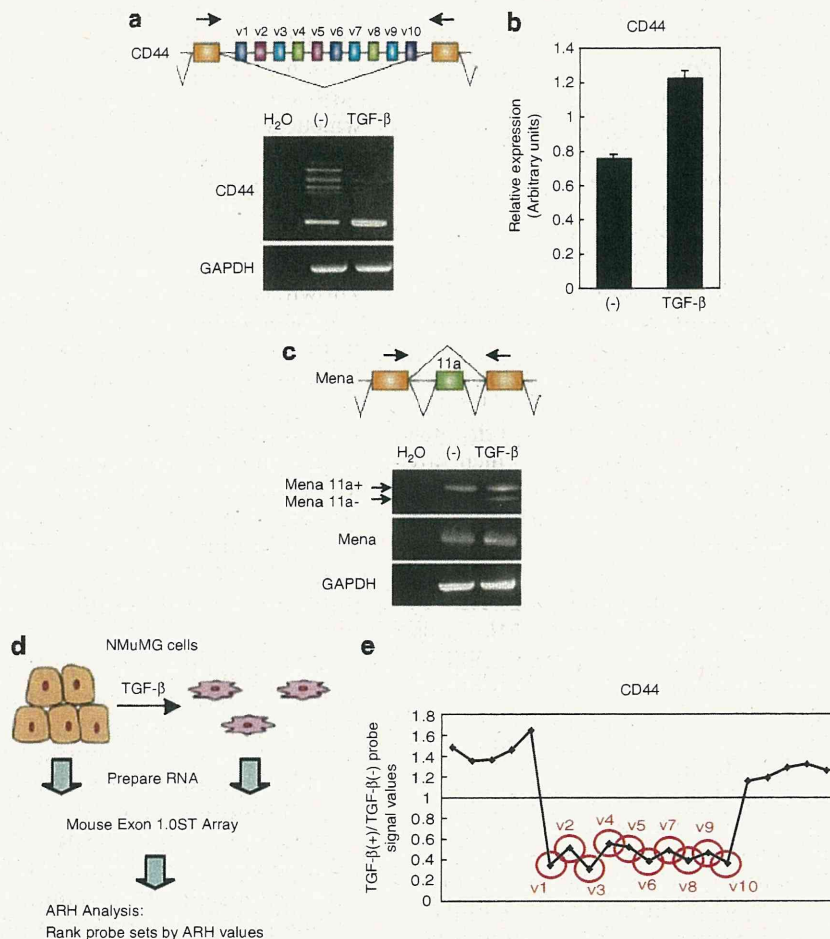
Figure 1 Changes in alternative splicing during TGF-β-induced EMT. (**a**) Changes in alternative splicing of CD44. Specific primers to detect v1-v10 variants of CD44 are shown as arrows (top panel). GAPDH was used as internal control. (**b**) The total level of CD44 mRNA was evaluated by quantitative RT–PCR analysis. (**c**) Specific primers to detect splicing variants of *Mena* are shown as arrows (top panel). GAPDH was used as internal control. (**d**) NMuMG cells treated with TGF-β for 24 h were prepared for Mouse Exon 1.0 ST Array. The ARH method was adapted to identify candidate genes at the exon level whose expressions changed during EMT. (**e**) The ratio of expression changes of each exon calculated by probe signal value in CD44 is shown. Red circles indicate the exons whose probe signals were altered by TGF-β treatment and reported to be spliced by ESRPs (Warzecha *et al.*, 2009a).

gradually decreased until 24 h upon TGF-β stimulation, with the expression profile similar to that of E-cadherin and reciprocal to that of δEF1 and SIP1 (Figure 3a). To evaluate the mechanism of reciprocal regulation between δEF1/SIP1 and ESRP2 expression, we prepared the ESRP2 promoter region from NMuMG cells by a PCR-based strategy. The activity of ESRP2 promoter in NMuMG cells was remarkably repressed by constitutively active mutant of TβR-I (caTβR-I), δEF1 and SIP1. δEF1 overexpression had a stronger effect than SIP1 overexpression, probably because the protein levels of transfected SIP1 were much lower than those of δEF1 as determined by immunoblot analysis (Figure 3b and Supplementary Figure S3a). When we infected the cells with adenoviral vector encoding either δEF1 or SIP1, δEF1 or SIP1 each reduced the expression of endogenous ESRP2 mRNA with equivalent efficiencies (Figure 3c).

To determine whether δEF1 and SIP1 interact with the promoter regions of ESRP2, we performed chromatin immunoprecipitation (ChIP) assays in NMuMG cells after TGF-β treatment. The quality of commercially available anti-δEF1 antibody was appropriate for ChIP assays, whereas that of anti-SIP1 antibodies was not suitable for this assay. Thus, we overexpressed FLAG-tagged SIP1 in NMuMG cells and immunoprecipitated it with anti-FLAG antibody. In the absence of TGF-β, the level of δEF1 expression was very low and thus insufficient for ChIP (Figure 3d). After treatment with TGF-β, interactions of δEF1 with DNA fragments of the ESRP2 promoter in NMuMG and EpRas cells (Figure 3d, left and data not shown) and the ESRP1 promoter in EpRas cells (Figure 3d, right) were observed. Moreover, SIP1 also interacted with the ESRP2 and ESRP1 promoters, whereas neither δEF1 nor SIP1 associated with hemoglobin β gene (HBB) promoter that was used as a negative control (Figure 3d). In the competition assays of ChIP, overexpression of FLAG-SIP1 reduced the interaction of endogenous δEF1
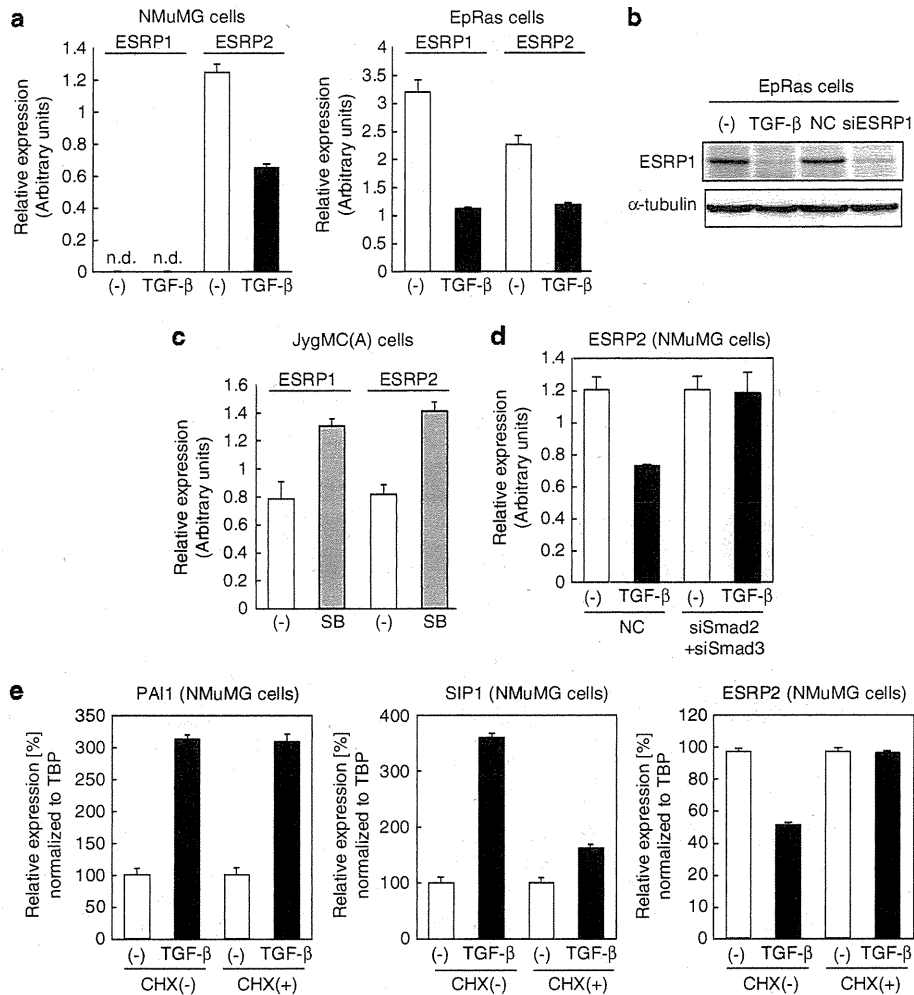
Figure 2 Requirement of *de novo* protein synthesis for downregulation of ESRP2 by TGF-β. (a) Effect of TGF-β on the expression of ESRPs in NMuMG cells (left) and EpRas cells (right) was examined by quantitative RT–PCR analysis. n.d., not detected. (b) After treatment of EpRas cells with TGF-β or transfection with ESRP1 siRNA, the levels of ESRP1 were evaluated by immunoblot analysis. α-tubulin was used as a loading control. (c) JygMC(A) cells were treated with 10 μM of TβR-I inhibitor (SB431542) for 48 h. The levels of ESRP1 and ESRP2 were evaluated by quantitative RT–PCR analysis. SB, SB431542. (d) NMuMG cells transfected with both Smad2 and Smad3 siRNAs were stimulated with 1 ng/ml TGF-β for 24 h, and then examined by quantitative RT–PCR analysis for the expression levels of ESRP2. NC, control siRNA. (e) NMuMG cells pretreated with 3 μM cycloheximide (CHX) for 1 h were stimulated with 1 ng/ml TGF-β for 24 h, and examined by quantitative RT–PCR analysis for PAI1 (left), SIP1 (center) and ESRP2 levels (right).

with the ESRP2 promoter (Supplementary Figure S3b), suggesting that δEF1 family proteins recognize the same binding regions of ESRP2 promoter. Overall, these findings indicate that δEF1 and SIP1 are preferentially recruited to the promoter region of ESRPs, and that they suppress the transcription of ESRPs in response to TGF-β treatment.

As double knockdown of δEF1 and SIP1 is necessary to block the E-cadherin repression by TGF-β (Shiraki-hara *et al.*, 2007), we next analyzed the TGF-β-mediated ESRP2 repression in NMuMG cells in which both δEF1 and SIP1 were silenced using their specific siRNAs (Figure 3e). TGF-β treatment induced the expression of δEF1 and SIP1 mRNAs by about three-fold after 48 h and repressed the expression of ESRP2. In the cells transfected with either δEF1 or SIP1 siRNA alone,

TGF-β-mediated ESRP2 repression was only partially blocked; however, transfection with both δEF1 and SIP1 siRNAs completely abolished the TGF-β-mediated ESRP2 repression (Figure 3e). The δEF1/SIP1-mediated ESRP repression was also detected in EpRas cells (Supplementary Figure S3c). Therefore, similar to the repression of E-cadherin, the transcription of ESRPs is accumulatively regulated by the δEF1 family proteins during EMT by TGF-β.

Switching between FGFR isoforms by ESRPs during TGF-β-induced EMT
As we have previously reported (Shirakihara *et al.*, 2011), FGFR1 upregulated by TGF-β in NMuMG cells was the mesenchymal isoform, that is, FGFR1IIIc,
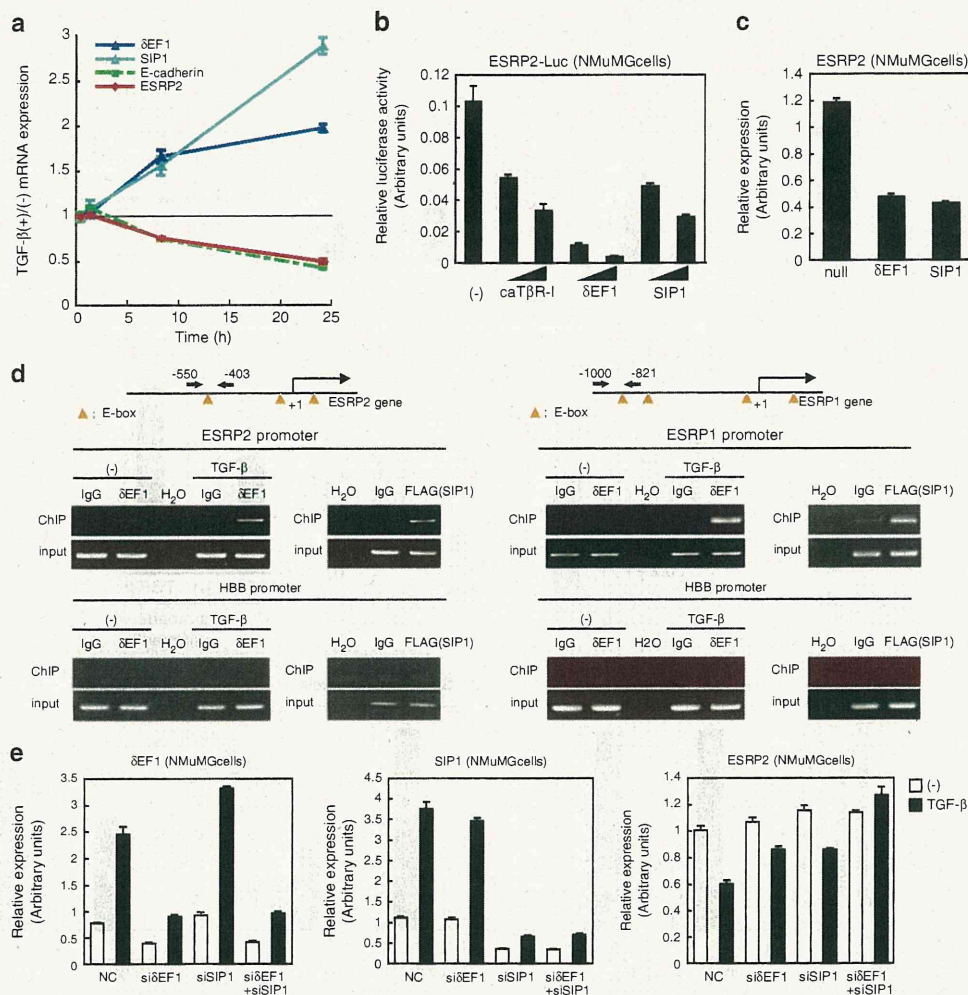
Figure 3 Regulation of ESRP2 expression by δEF1 and SIP1. (**a**) After treatment with 1 ng/ml of TGF-β, the kinetics of ESRP2, δEF1, SIP1 and E-cadherin expressions were examined in NMuMG cells by quantitative RT–PCR analysis. The ratio of the mRNA levels in TGF-β-treated cells as compared with that in non-treated cells is shown. (**b**) NMuMG cells were transfected with mouse ESRP2 promoter-reporter construct (ESRP2-Luc) in combination with various amounts of caTβR-I, δEF1 and SIP1 plasmids. At 48 h after transfection, cells were harvested and assayed for luciferase activities. (**c**) mRNA levels of ESRP2 in NMuMG cells infected with null, δEF1 or SIP1 adenoviruses were determined by quantitative RT–PCR. (**d**) ChIP analysis was performed using NMuMG and EpRas cells in the presence or absence of 1 ng/ml TGF-β. FLAG-SIP1 adenovirus was infected into NMuMG and EpRas cells 24 h before ChIP analysis. Endogenous δEF1 and FLAG-SIP1 were immunoprecipitated with anti-δEF1 antibody and with anti-FLAG antibody, respectively. Eluted DNAs from NMuMG cells and from EpRas cells were subjected to conventional PCR for ESRP2 promoter (left) and for ESRP1 promoter (right), respectively. HBB promoter was used as negative control. Primers used are shown as arrows. (**e**) NMuMG cells transfected with siRNA against δEF1, SIP1, or both (siδEF1 + siSIP1) were stimulated with 1 ng/ml TGF-β for 48 h and examined by quantitative RT–PCR analysis for δEF1 (left), SIP1 (center) and ESRP2 levels (right). NC, control siRNA.

whereas the FGFR2 downregulated by TGF-β was the epithelial isoform, that is, FGFR2IIIb (Figure 4a). Further, isoform switching of FGFR1 and FGFR2 was also observed in EpRas cells, in which both ESRP1 and ESRP2 were endogenously expressed (Figures 2a and 4b). Because TGF-β downregulated the total levels of FGFR2, the TGF-β-mediated induction of the IIIc isoform of FGFR2 was not clearly detected in both cells (Figures 4a and b). When ESRP2 was silenced by its specific siRNAs in NMuMG cells, ESRP2 siRNA changed the FGFR2IIIb isoform to FGFR2IIIc isoform without appearance of FGFR1IIIc in the absence of TGF-β (Figure 4c), suggesting that the TGF-β-mediated

conversion of FGFR2IIIb into FGFR1IIIc requires ESRPs as well as other unidentified transcriptional factor(s). In addition, transfection with both ESRP1 and ESRP2 siRNAs in EpRas cells resulted in the expression of IIIc isoform of FGFR2 as well as that of FGFR1 (Figure 4d). Taken together, these findings suggest that TGF-β increases FGFR1 expression and decreases FGFR2 expression, leading to the conversion of the IIIb isoform into the IIIc isoform of FGFRs through alternative splicing by ESRPs.

We next performed gain-of-function experiments after achieving ectopic expression of FLAG-tagged ESRP2. After TGF-β treatment, the FGFR1IIIc isoform was
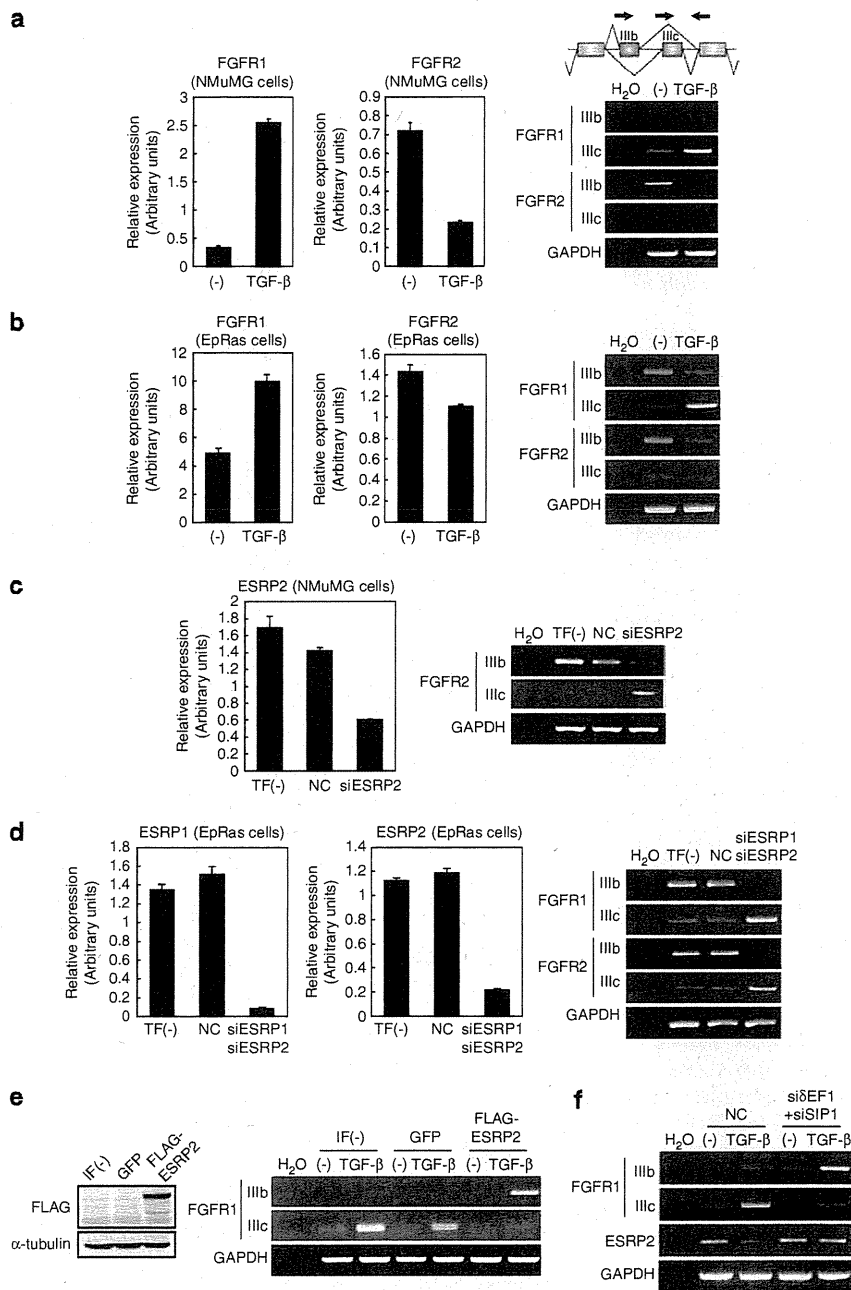
Figure 4 Isoform switching of FGFRs induced by TGF-β. (a) NMuMG cells were treated with 1 ng/ml TGF-β for 24 h and the expression of FGFR1 (left) and FGFR2 (center) was determined by quantitative RT–PCR. Expression of FGFR isoforms was analyzed by conventional RT–PCR using specific primers for IIIb or IIIc (right). (b) After EpRas cells were treated with 1 ng/ml TGF-β, the total levels of FGFR1 (left) and FGFR2 (center) and expression of FGFR isoforms (right) were examined. (c) NMuMG cells transfected with siRNA against mouse ESRP2 (siESRP2) were incubated for 48 h, and then analyzed by quantitative RT–PCR to determine the levels of endogenous ESRP2 (left). Expression of FGFR2 isoform was analyzed by conventional RT–PCR (right). TF(−), no transfection; NC, control siRNA. (d) EpRas cells transfected with siRNAs against both ESRP1 (siESRP1) and ESRP2 (siESRP2) were incubated for 48 h, and analyzed by quantitative RT–PCR to determine the levels of endogenous ESRP1 (left) and ESRP2 (center). Expression of FGFR isoforms was analyzed by conventional RT–PCR (right). TF(−), no transfection; NC, control siRNA. (e) NMuMG cells infected with GFP or FLAG-ESRP2 lentiviruses were treated with TGF-β for 24 h and analyzed by immunoblot analysis (left) and conventional RT–PCR to determine the levels of IIIb and IIIc isoforms of FGFR1 (right). IF(−), no infection. (f) After NMuMG cells were treated with 1 ng/ml TGF-β for 48 h or transfected with both δEF1 and SIP1 siRNAs, conventional RT–PCR were performed to detect expression of FGFR1 isoforms. NC, control siRNA

expressed in control or GFP-transfected cells, whereas it was replaced with the IIIb isoform in ESRP2-overexpressed cells (Figure 4e). Importantly, when

δEF1 and SIP1 were silenced by their specific siRNAs in NMuMG cells, treatment with TGF-β did not result in the replacement of the IIIc isoform of FGFR1, due to

de-repression of the ESRP2 (Figure 4f). Switching of responses to FGF ligands was also confirmed by phosphorylation of Erk in NMuMG cells (Supplementary Figures S4a–f). These findings, thus, suggest that isoform switching of functional FGFRs through TGF-β-induced alternative splicing is mediated by δEF1/SIP1-repressed ESRPs.

Regulation of ESRP expression by δEF1 and SIP1 in human breast cancer cells

TGF-β-induced EMT appears to correlate with the progression of various cancers, especially breast cancer (Padua and Massague, 2009). We examined the expression of ESRPs and δEF1/SIP1 as well as that of other EMT regulators, including Snail, Twist and Slug, in 23 human breast cancer cell lines. As previously reported, the expression of ESRPs was correlated with E-cadherin expression (Supplementary Figure S5) (Warzecha et al., 2009a,b). Interestingly, the expression levels of δEF1 and SIP1 mRNAs in these cell lines were inversely correlated to those of ESRPs (Figure 5a). However, the expression levels of neither Snail, Slug nor Twist were significantly correlated with those of ESRPs in human breast cancer cells used in our study (Supplementary Figure S5). Importantly, most of the cell lines with high levels of δEF1 and SIP1 expression and low levels of ESRPs expression appeared to be categorized into the 'basal-like' subtype of breast cancer (Charafe-Jauffret et al., 2006; Neve et al., 2006; Yamaguchi et al., 2008). In contrast, most of the cell lines with low levels of δEF1 and SIP1 expression and high levels of ESRPs expression were categorized into the 'luminal' subtype of breast cancer. Among the 23 cell lines, we selected several cell lines and confirmed the expression of FGFR isoforms by RT–PCR. CRL1500 and UACC893 cells, which expressed low δEF1/SIP1 levels and high ESRP1/2 levels, exhibited constitutive expression of only IIIb isoforms of FGFR (Figure 5b). On the other hand, MDA-MB-231, MDA-MB-157, Hs578T, HCC1395 and BT549 cells, with low expression of ESRPs and high expression of δEF1/SIP1, expressed only IIIc isoforms of FGFRs (Figure 5b). Moreover, double knockdown of δEF1 and SIP1 increased the expression of ESRP1 and ESRP2 in MDA-MB231 and BT549 cells (Figure 5c), indicating that δEF1 and SIP1 down-regulate ESRP expression in human breast cancer cells.

We next examined whether δEF1/SIP1 and ESRPs are reciprocally expressed in human breast tumors. Primary tumor tissues from cancer patients were subjected to immunohistochemical analyses with anti-δEF1 and anti-ESRP1 antibodies. The quality of anti-ESRP2 antibodies obtained in our study was not suitable for immunohistochemical analyses. The samples analyzed showed positive ESRP1 and cytokeratin 19 (K19) staining in cancer cells in tumor nest, whereas δEF1 was not detected in typical tumor cells, especially those in the tumor nest, but it was clearly detected in stromal cells and spindle-shaped cells at the degenerated tumor nests (Figure 5d). Therefore, these findings suggest that the expression levels of ESRP and δEF1

are reciprocally controlled in tumor tissues and/or stroma tissues, which was consistent with the expression profiles in breast cancer cell lines.
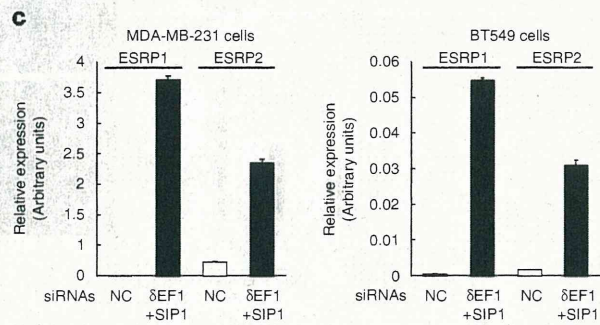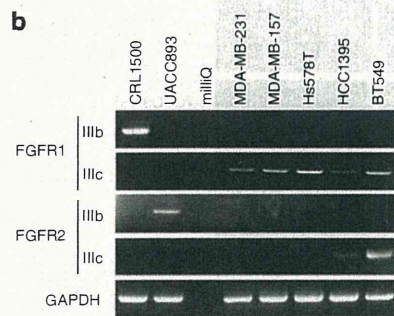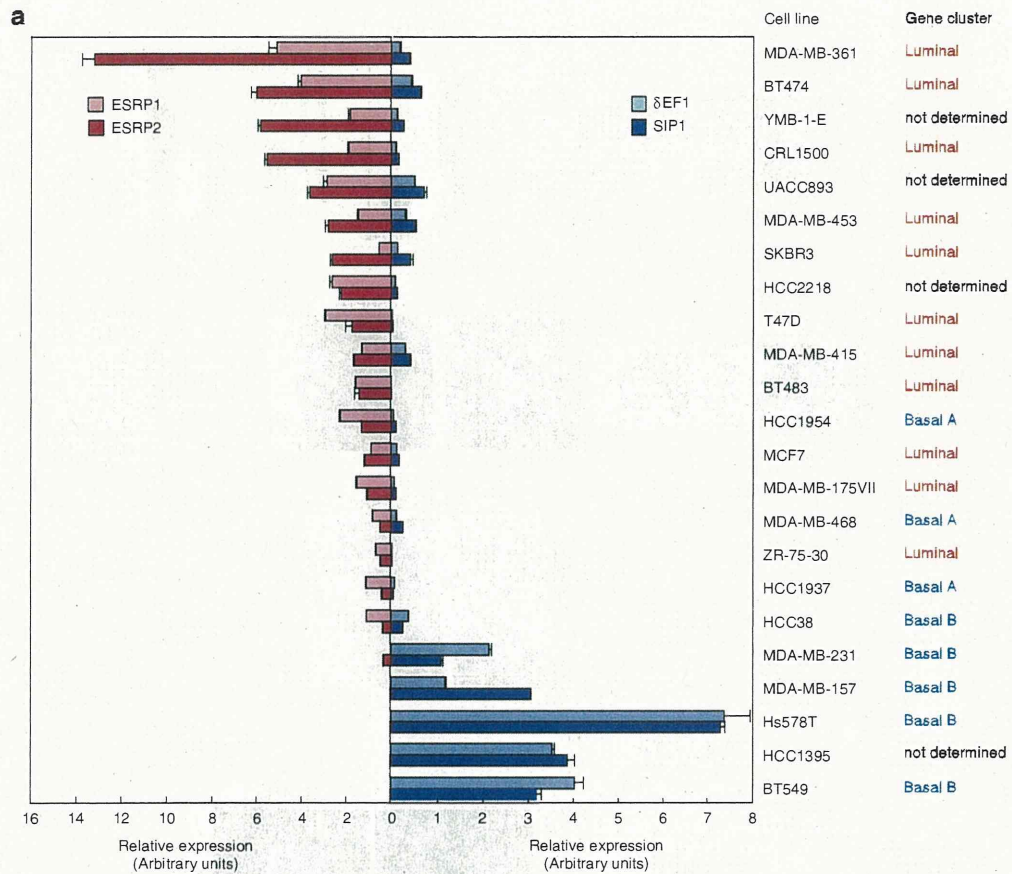
ESRPs attenuate malignant phenotypes of cancer cells as well as EMT

MDA-MB-231 cells are morphologically classified as poorly differentiated carcinoma cells (Neve et al., 2006). We analyzed the anchorage-independent growth of MDA-MB-231 cells by cultivating the cells in soft agar. As shown in Figure 6a, these cells showed anchorage-independent growth, whereas the cells overexpressing ESRPs failed to efficiently proliferate in soft agar. Overexpression of ESRPs also switched the isoform expression of FGFR1 from IIIc to IIIb in MDA-MB-231 cells (Supplementary Figure S6a). The expression of E-cadherin was upregulated at the mRNA and protein levels in cells overexpressing ESRPs (Figures 6b, d and e), whereas reorganization of actin stress fiber and expressions of EMT regulators and mesenchymal marker proteins, including fibronectin and N-cadherin, were not significantly affected by ESRP overexpression (Figure 6e, Supplementary Figures S6b and c). In addition, morphology of the cells overexpressing ESRPs was altered to a cobblestone-like shape (Figure 6c), suggesting that ESRPs partially restored the well-differentiated phenotype in cells with a poorly differentiated phenotype. Moreover, these effects of ESRPs were also confirmed in NMuMG cells, in which the overexpression of ESRP2 restored TGF-β-mediated alteration of morphology and downregulation of E-cadherin (Figures 6f, g and h). Similar to MDA-MB-231 cells, ESRP overexpression failed to affect the expression of mesenchymal marker proteins and reorganization of actin stress fiber (Supplementary Figures S6d and e). These findings thus suggest that ESRPs attenuate the EMT phenotype mainly through upregulation of E-cadherin.

Discussion

Roles of ESRPs in alteration in splicing during TGF-β-induced EMT

By comparing our data with the published database of the exon-array data of ESRP1/2-silenced PNT2 cells using high ARH scores ($P < 0.01$), a subset of genes in NMuMG cells overlapped with those in PNT2 cells (Supplementary Table 2). Recently, profiling of ESRP-regulated splicing using a further sensitive analysis was reported (Warzecha et al., 2010). In the report, Affymetrix human exon junction arrays were performed to profile splicing changes in response to ectopic expression of ESRP1 in MDA-MB-231 cells and knockdown of ESRP1 and ESRP2 in PNT2 cells. They identified 310 genes in MDA-MB-231 cells and 385 genes in PNT2 cells as ESRP-dependent targets of alternative splicing. When they were compared with our gene list of NMuMG cells ($P < 0.01$), 55 genes in MDA-MB-231 cells and 92 genes in PNT2 cells matched our
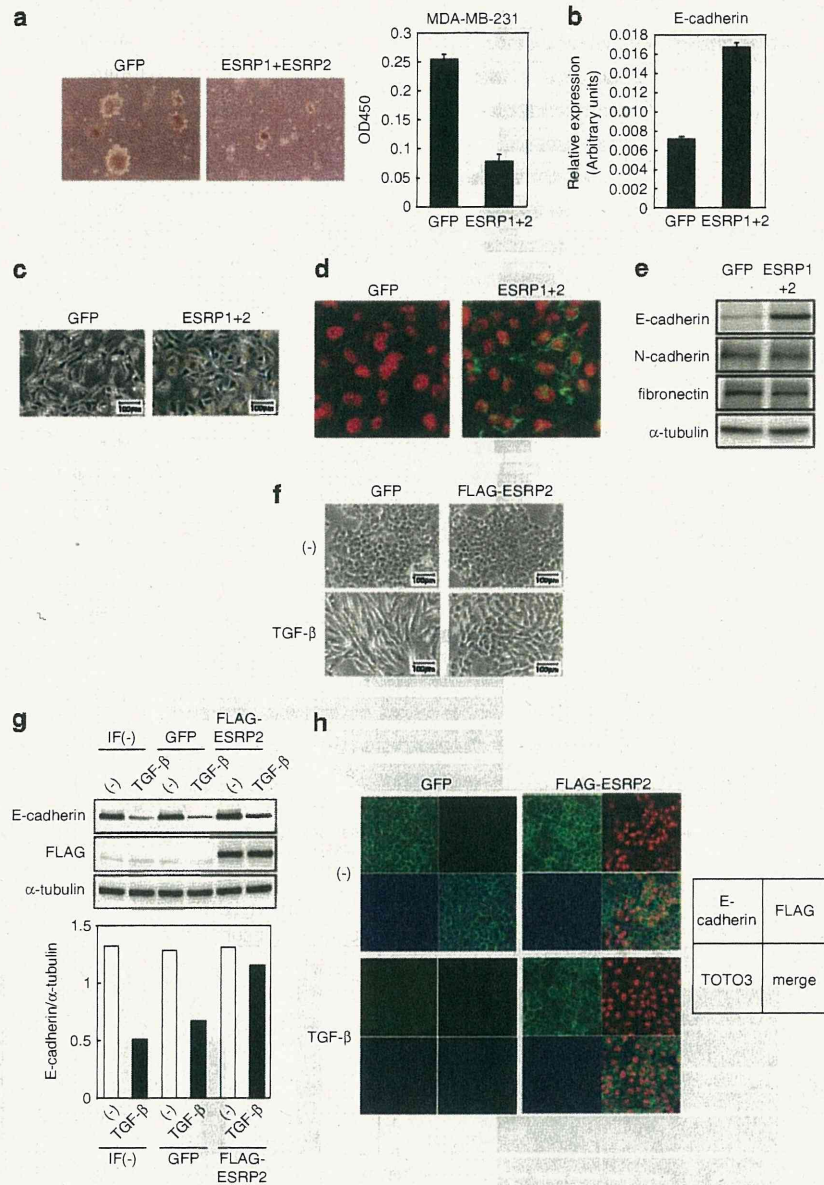
a

Cell line	Gene cluster
MDA-MB-361	Luminal
BT474	Luminal
YMB-1-E	not determined
CRL1500	Luminal
UACC893	not determined
MDA-MB-453	Luminal
SKBR3	Luminal
HCC2218	not determined
T47D	Luminal
MDA-MB-415	Luminal
BT483	Luminal
HCC1954	Basal A
MCF7	Luminal
MDA-MB-175VII	Luminal
MDA-MB-468	Basal A
ZR-75-30	Luminal
HCC1937	Basal A
HCC38	Basal B
MDA-MB-231	Basal B
MDA-MB-157	Basal B
Hs578T	Basal B
HCC1395	not determined
BT549	Basal B

ESRP1
ESRP2
δEF1
SIP1

Relative expression (Arbitrary units)
Relative expression (Arbitrary units)

b

c

d

Figure 6 ESRPs attenuate malignant phenotypes of cancer cells. (**a–e**) MDA-MB-231 cells were infected with lentiviruses encoding ESRP1 and ESRP2. The cells were examined for anchorage-independent growth in soft agar (left in **a**) and quantified (right in **a**). Expression of E-cadherin in the cells was evaluated by quantitative RT–PCR (**b**), immunohistochemical (**d**) and immunoblot (**e**) analyses. (**c**) Morphology of the cells was analyzed by phase-contrast microscopy (**d**). α-tubulin levels were monitored as a loading control (**e**). (**f–h**) NMuMG cells infected with lentivirus encoding GFP or FLAG-ESRP2 were treated with TGF-β for 36 h. The cells were analyzed by phase-contrast microscopy (**f**), immunoblot analyses with the indicated antibodies (**g**), and immunohistochemical analyses with anti-E-cadherin (green in **h**) and anti-FLAG (red in **h**) antibodies, and by TOTO3 to detect nuclei (blue in **h**). α-tubulin levels were monitored as a loading control. Ratio of E-cadherin to α-tubulin is shown at bottom (**g**). IF(−), no infection.

Figure 5 Expression profiles of ESRP1/2 and δEF1/SIP1 in breast cancer cells. (**a**) mRNA levels of the expression of ESRP1, ESRP2, δEF1 and SIP1 were determined by quantitative RT–PCR and compared among 23 human breast cancer cell lines. Gene cluster shown is reported by Neve et al. (2006) and Charafe-Jauffret et al. (2006). Basal A subtype reveals basal-like signature with basal cytokeratin (K5/K14) positive, and basal B subtype exhibits a stem-cell like expression profile with vimentin positive and may reflect the clinical triple-negative tumor type (Neve et al., 2006). (**b**) The expression of FGFRs isoforms in human breast cancer cell lines was determined by conventional RT–PCR. (**c**) MDA-MB-231 and BT549 cells were transfected with siRNAs against δEF1 and SIP1, and mRNA levels of ESRP1 and ESRP2 were examined by quantitative RT–PCR. NC, control siRNA. (**d**) Representative images of hematoxylin and eosin (HE) staining and immunohistochemical staining of cytokeratin 19 (K19), ESRP1, and δEF1 in primary tumor samples from breast cancer patients are shown (# 1 and 2).

gene list of NMuMG cells. Although it is difficult to further evaluate these data, due to the differences in species and tissues of the cells lines, these findings suggest that ESRPs play crucial roles in alteration in splicing variants during TGF-β-induced EMT.

Regulation of FGFRs by TGF-β at the levels of transcription and alternative splicing

Splicing of the second half of the third Ig-like domain of the FGFRs has been well documented (Eswarakumar et al., 2005). ESRPs were identified through the screening of the proteins that regulate the splicing of FGFRs (Warzecha et al., 2009a, b). We have recently reported that TGF-β induces isoform switching of FGFRs from the IIIb to IIIc type by alternative splicing during EMT in NMuMG cells, which results in enhanced EMT through the cooperative action of TGF-β and FGF-2 (Shirakihara et al., 2011). NMuMG cells predominantly expressed FGFR2IIIb in the resting state. TGF-β repressed the expression of FGFR2IIIb isoform and induced the expression of the FGFR1IIIc isoform, but not that of the FGFR2IIIc (Figure 4a). Importantly, overexpression of ESRP2 in TGF-β-treated NMuMG cells led to an increase in FGFR1IIIb isoform (Figure 4e), and δEF1 and SIP1 siRNAs did not affect the upregulation of FGFR1 (Figure 4f). These findings suggest that δEF1 and SIP1 are dispensable in the TGF-β-mediated transcriptional regulation of FGFR1. Therefore, isoform switching of FGFRs during TGF-β-induced EMT requires ESRPs and other unidentified transcriptional factor(s) that are not regulated by δEF1/SIP1.

Splicing profiles of CD44 and Mena were also changed by ESRP2 siRNA (Supplementary Figures S7a and b). As described above, treatment by TGF-β alone induced partial EMT with about 50% reduction of ESRP2 mRNA (Figure 2a). Thus, addition of FGF-2 in TGF-β-treated cells further repressed the levels of ESRP2 mRNA and in turn changed the profile of alternative splicing of Mena (Supplementary Figure S7c). When ESRP2 was knocked down in TGF-β-treated cells, Mena was almost completely altered to its splicing variant (Mena 11a-) (Supplementary Figure S7d). These findings, therefore, suggest that TGF-β stimulation elicits partial EMT with repression of ESRP2 to about 50%, and that further reduction of ESRP2 expression induces enhanced EMT with aggressive phenotypes of mesenchyme.

Attenuation of EMT phenotype by ESRPs

Human breast cancer MDA-MB-231 cells are classified as poorly differentiated carcinoma cells, and express low levels of ESRP1/2 and high levels of δEF1/SIP1. Overexpression of ESRPs upregulated E-cadherin expression without affecting the levels of δEF1 and SIP1 (Figures 6b–e, and Supplementary Figure S6c). Among other EMT regulators, expression of Snail and Slug was not affected by ESRPs, whereas that of E47 and Twist was not detected in the cells (Supplementary Figure S6c and data not shown), suggesting that restoration of E-cadherin by ESRPs is not induced by de-repression of the EMT regulators. In addition, ESRP2 overexpression

failed to downregulate mesenchymal-marker proteins and restore reorganization of actin stress fiber in MDA-MB-231 and TGF-β-treated NMuMG cells (Figures 6e, Supplementary Figures S6b, d and e). In the present study, some of polarity and adhesion proteins, including p120 catenin and scribbled, are regulated at splicing levels by ESRPs. Thus, alternative splicing variants of these proteins may regulate unidentified E-cadherin inducers or epithelial regulators, and alter the cells from mesenchymal to epithelial phenotype through increase in E-cadherin expression.

Regulation of ESRP expression in other types of cancer

δEF1 and SIP1 are necessary for TGF-β-induced EMT in NMuMG cells and in some breast cancer cells (Shirakihara et al., 2007; Gregory et al., 2008). Intriguingly, they were not upregulated by TGF-β and dispensable for TGF-β-induced EMT in pancreatic cancer Panc-1 cells, in which Snail was involved in TGF-β-induced EMT (Horiguchi et al., 2009). Moreover, Twist induced EMT in human mammary epithelial HMLE cells (Yang et al., 2004). Thus, expression of each EMT regulator appears to be variously regulated in the cells that have undergone EMT, depending on cell or tissue specificity. EMT regulators are not good markers to detect cells that have undergone EMT, because in certain cells it is difficult to determine which regulators specifically and preferentially contribute to EMT. However, ESRPs were repressed by Snail and Twist in certain cells that had undergone EMT, including Panc-1 cells (Supplementary Figure S8) and HMLE cells (Warzecha et al., 2009a, b), respectively, and the expression of ESRPs was inversely correlated with progression of breast cancer (Figure 5a). Therefore, these findings suggest that ESRPs, rather than EMT regulators, may be useful negative markers for detecting cells that have undergone EMT or cancer cells with more aggressive phenotypes.

Expression of δEF1/SIP1 and ESRPs in the 'basal-like' and 'luminal' types of breast cancer cells

Our findings on a panel of 23 human breast cancer cell lines revealed an important phenomenon that the expression levels of ESRPs are reciprocally controlled by the expression levels of δEF1 family proteins. Importantly, most of the cell lines with high levels of δEF1 and SIP1 expression and low levels of ESRP expression were categorized into the 'basal-like' subtype of breast cancer (Charafe-Jauffret et al., 2006; Neve et al., 2006; Yamaguchi et al., 2008). Thus, elevated expression of δEF1 and SIP1 appears to correlate with aggressive phenotypes and poor prognosis of cancer patients, which are most likely due to the reinforced invasive and metastatic properties of tumor cells via EMT. In contrast, most of the cell lines with low levels of δEF1 and SIP1 expression and high levels of ESRPs expression were categorized into the 'luminal' subtype of breast cancer. Thus, δEF1 and SIP1 are specifically expressed in 'basal-like' subtype and ESRPs are specifically expressed in 'luminal' subtype of breast cancer cells. Although some of the luminal-type breast cancer cells expressed high levels of Snail or Twist

mRNAs, it is still unknown why these EMT regulators failed to affect E-cadherin expression. In addition to mRNA profiling, determination of the protein levels of the EMT regulators will be required in the future.

Materials and methods

Cell culture, reagents and antibodies

All cells used in the present study were cultured as described previously (Shirakihara *et al.*, 2011). Recombinant human TGF-β1 was obtained from R&D Systems (Minneapolis, MN, USA). SB431542 was form Sigma-Aldrich (St Louis, MO, USA). Mouse monoclonal anti-FLAG M2, anti-α-tubulin and anti-ESRP1 antibodies were purchased from Sigma-Aldrich. Rabbit monoclonal anti-keratin 19 and polyclonal δEF1 antibodies were purchased from Epitomics (Burlingame, CA, USA) and Novus Biologicals (Littleton, CO, USA), respectively. Mouse anti-E-cadherin antibody was from BD Transduction Laboratories (Lexington, KY, USA).

RNA extraction, microarray and RT–PCR analyses

Total RNA was purified using the RNeasy Mini Kit (Qiagen, Valencia, CA, USA) and used to perform microarray, conventional RT–PCR and quantitative RT–PCR analyses. Values were normalized to mouse TATA binding protein (TBP) or human hypoxanthine phosphoribosyltransferase 1. The primer sequences are shown in Supplementary Table 3. Oligonucleotide microarray analysis was performed using GeneChip Mouse Exon 1.0 ST Array (Affymetrix) according to the manufacturer's instructions. The ARH method was used to identify exons differentially expressed between non-treated and TGF-β-treated NMuMG cells (Rasche and Herwig, 2010). Exon-array data are available at Gene Expression Omnibus (GSE28184).

DNA construction and generation of lentiviruses

Mouse ESRP2 promoter, containing −1000 to +200 base pairs from transcription start site, was cloned by PCR using genomic DNA of NMuMG cells. The purified PCR fragment was cloned into pGL4 vector (Promega, Madison, WI, USA). Human ESRP1 and mouse ESRP2 were cloned by PCR using cDNA of A431 and NMuMG cells. All constructs were confirmed by sequencing. The mouse δEF1 and SIP1 cDNAs, and the adenoviral vector encoding δEF1 or SIP1 epitope-tagged with FLAG at their N-termini were described previously (Shirakihara *et al.*, 2007). We used a lentiviral expression system to establish stable expression of ESRP2 in NMuMG cells (NMuMG-ESRP2) and that of ESRP1/2 in MDA-MB-231 cells (Horiguchi *et al.*, 2009).

RNA interference

Transfection of siRNA was performed according to the protocol recommended for HiPerfect (Qiagen) or RNAiMAX

(Invitrogen, Carlsbad, CA, USA). NMuMG cells were transiently transfected with siRNAs against mouse δEF1 (Stealth RNAi MSS210696; Invitrogen), mouse SIP1 (Stealth RNAi MSS216412; Invitrogen), mouse ESRP1 (Stealth RNAi MSS209488; Invitrogen), or mouse ESRP2 (Stealth RNAi MSS246490; Invitrogen). Human breast cancer cells were transiently transfected with siRNAs against human δEF1 (Stealth RNAi HSS110549; Invitrogen) and human SIP1 (Stealth RNAi HSS114854; Invitrogen). The final concentration of the siRNAs used was 20 nM. At 12 h after transfection, 1 ng/ml TGF-β was added and cultured for an additional 48 h.

Immunoblotting, luciferase assays, ChIP and immunohistochemistry analyses of tumor sample

The procedures used for immunoblotting, immunofluorescence, luciferase assays and ChIP were as previously described (Horiguchi *et al.*, 2009; Koinuma *et al.*, 2009). Formalin-fixed, paraffin-embedded primary breast tumor tissues were obtained as a part of routine clinical management of patients with breast cancer at the Hospital of University of Yamanashi. Hematoxylin and eosin-stained sections were examined for regions that contained tumor cells and stroma, which were then analyzed as serial sections for anti-δEF1, ESRP1 and K19 antibodies. All studies were conducted using the protocol approved by the Ethics Committee of the University of Yamanashi.

Colony-formation assay in soft agar

Agar (Nacalai Tesque, Kyoto, Japan) was dissolved with culture medium to a final concentration of 0.5% in six-well plates. Cells were seeded at a density of 3×10^4 cells per well in 0.3% agar. The cells were covered with culture media for 3 weeks. Cell viability was measured using Cell Count Reagent SF (Nacalai Tesque). The reagent was added in the media and incubated for 60 min. The aliquot was taken and colorimetrically measured at 450–650 nm wavelengths.

Conflict of interest

The authors declare no conflict of interest.

Acknowledgements

References

Blencowe BJ. (2006). Alternative splicing: new insights from global analyses. *Cell* **126**: 37–47.

Chaffer CL, Dopheide B, Savagner P, Thompson EW, Williams ED. (2007). Aberrant fibroblast growth factor receptor signaling in bladder and other cancers. *Differentiation* **75**: 831–842.

Charafe-Jauffret E, Ginestier C, Monville F, Finetti P, Adelaide J, Cervera N *et al.* (2006). Gene expression profiling of breast

cell lines identifies potential new basal markers. *Oncogene* **25**: 2273–2284.

Coumoul X, Deng CX. (2003). Roles of FGF receptors in mammalian development and congenital diseases. *Birth Defects Res C Embryo Today* **69**: 286–304.

Dutertre M, Lacroix-Triki M, Driouch K, de la Grange P, Gratadou L, Beck S *et al.* (2010). Exon-based clustering of murine breast

tumor transcriptomes reveals alternative exons whose expression is associated with metastasis. *Cancer Res* **70**: 896–905.

Ehata S, Hanyu A, Hayashi M, Aburatani H, Kato Y, Fujime M et al. (2007). Transforming growth factor-β promotes survival of mammary carcinoma cells through induction of antiapoptotic transcription factor DEC1. *Cancer Res* **67**: 9694–9703.

Eswarakumar VP, Lax I, Schlessinger J. (2005). Cellular signaling by fibroblast growth factor receptors. *Cytokine Growth Factor Rev* **16**: 139–149.

Gregory PA, Bert AG, Paterson EL, Barry SC, Tsykin A, Farshid G et al. (2008). The miR-200 family and miR-205 regulate epithelial to mesenchymal transition by targeting ZEB1 and SIP1. *Nat Cell Biol* **10**: 593–601.

Horiguchi K, Shirakihara T, Nakano A, Imamura T, Miyazono K, Saitoh M. (2009). Role of Ras signaling in the induction of Snail by transforming growth factor-β. *J Biol Chem* **284**: 245–253.

Hoshino Y, Katsuno Y, Ehata S, Miyazono K. (2011). Autocrine TGF-β protects breast cancer cells from apoptosis through reduction of BH3-only protein, Bim. *J Biochem* **149**: 55–65.

Kalluri R, Weinberg RA. (2009). The basics of epithelial-mesenchymal transition. *J Clin Invest* **119**: 1420–1428.

Koinuma D, Tsutsumi S, Kamimura N, Taniguchi H, Miyazawa K, Sunamura M et al. (2009). Chromatin immunoprecipitation on microarray analysis of Smad2/3 binding sites reveals roles of ETS1 and TFAP2A in transforming growth factor β signaling. *Mol Cell Biol* **29**: 172–186.

Lee B, Brown K, Hathout Y, Seo J. (2008). GOTreePlus: an interactive gene ontology browser. *Bioinformatics* **24**: 1026–1028.

Licatalosi DD, Darnell RB. (2010). RNA processing and its regulation: global insights into biological networks. *Nat Rev Genet* **11**: 75–87.

Matlin AJ, Clark F, Smith CW. (2005). Understanding alternative splicing: towards a cellular code. *Nat Rev Mol Cell Biol* **6**: 386–398.

Miyazono K. (2009). Transforming growth factor-β signaling in epithelial-mesenchymal transition and progression of cancer. *Proc Jpn Acad Ser B Phys Biol Sci* **85**: 314–323.

Moustakas A, Heldin CH. (2007). Signaling networks guiding epithelial-mesenchymal transitions during embryogenesis and cancer progression. *Cancer Sci* **98**: 1512–1520.

Neve RM, Chin K, Fridlyand J, Yeh J, Baehner FL, Fevr T et al. (2006). A collection of breast cancer cell lines for the study of functionally distinct cancer subtypes. *Cancer Cell* **10**: 515–527.

Padua D, Massague J. (2009). Roles of TGFβ in metastasis. *Cell Res* **19**: 89–102.

Pan Q, Shai O, Lee LJ, Frey BJ, Blencowe BJ. (2008). Deep surveying of alternative splicing complexity in the human transcriptome by high-throughput sequencing. *Nat Genet* **40**: 1413–1415.

Philippar U, Roussos ET, Oser M, Yamaguchi H, Kim HD, Giampieri S et al. (2008). A Mena invasion isoform potentiates EGF-induced carcinoma cell invasion and metastasis. *Dev Cell* **15**: 813–828.

Rasche A, Herwig R. (2010). ARH: predicting splice variants from genome-wide data with modified entropy. *Bioinformatics* **26**: 84–90.

Shirakihara T, Horiguchi T, Miyazawa M, Ehata S, Shibata T, Morita I et al. (2011). TGF-β regulates isoform switching of FGF receptors and epithelial-mesenchymal transition. *EMBO J* **30**: 783–795.

Shirakihara T, Saitoh M, Miyazono K. (2007). Differential regulation of epithelial and mesenchymal markers by δEF1 proteins in epithelial mesenchymal transition induced by TGF-β. *Mol Biol Cell* **18**: 3533–3544.

Thiery JP, Acloque H, Huang RY, Nieto MA. (2009). Epithelial-mesenchymal transitions in development and disease. *Cell* **139**: 871–890.

Thiery JP, Sleeman JP. (2006). Complex networks orchestrate epithelial-mesenchymal transitions. *Nat Rev Mol Cell Biol* **7**: 131–142.

Wang ET, Sandberg R, Luo S, Khrebtukova I, Zhang L, Mayr C et al. (2008). Alternative isoform regulation in human tissue transcriptomes. *Nature* **456**: 470–476.

Wang GS, Cooper TA. (2007). Splicing in disease: disruption of the splicing code and the decoding machinery. *Nat Rev Genet* **8**: 749–761.

Warzecha CC, Jiang P, Amirikian K, Dittmar KA, Lu H, Shen S et al. (2010). An ESRP-regulated splicing programme is abrogated during the epithelial-mesenchymal transition. *EMBO J* **29**: 3286–3300.

Warzecha CC, Sato TK, Nabet B, Hogenesch JB, Carstens RP. (2009a). ESRP1 and ESRP2 are epithelial cell-type-specific regulators of FGFR2 splicing. *Mol Cell* **33**: 591–601.

Warzecha CC, Shen S, Xing Y, Carstens RP. (2009b). The epithelial splicing factors ESRP1 and ESRP2 positively and negatively regulate diverse types of alternative splicing events. *RNA Biol* **6**: 546–562.

Yamaguchi N, Ito E, Azuma S, Honma R, Yanagisawa Y, Nishikawa A et al. (2008). FoxA1 as a lineage-specific oncogene in luminal type breast cancer. *Biochem Biophys Res Commun* **365**: 711–717.

Yang J, Mani SA, Donaher JL, Ramaswamy S, Itzykson RA, Come C et al. (2004). Twist, a master regulator of morphogenesis, plays an essential role in tumor metastasis. *Cell* **117**: 927–939.

Supplementary Information accompanies the paper on the Oncogene website (http://www.nature.com/onc)

Structural differences in the osteocyte network between the calvaria and long bone revealed by three-dimensional fluorescence morphometry, possibly reflecting distinct mechano-adaptations and sensitivities

Akiko Himeno-Ando [a,b,c], Yuichi Izumi [b,c], Akira Yamaguchi [a,c,*], Tadahiro Iimura [a,c,*]

[a] Section of Oral Pathology, Graduate School of Medical and Dental Sciences, Tokyo Medical and Dental University, Japan
[b] Section of Periodontology, Graduate School of Medical and Dental Sciences, Tokyo Medical and Dental University, Japan
[c] Global Center of Excellence (GCOE) Program, International Research Center for Molecular Science in Tooth and Bone Diseases, Tokyo Medical and Dental University, Japan

ARTICLE INFO

ABSTRACT

The structural features of osteocytes and their cellular process network are thought to allow for mechanotransduction from the bone tissue to these cells. This study applied three-dimensional fluorescence microscopy to fixed and decalcified bone specimens to quantitatively compare the osteocytes and their networks between mouse parietal bone and tibia that are physiologically enforced by distinct mechanical loads. The subsequent morphometric analysis by the surface rendering of osteocyte cell bodies revealed the tibia to have relatively enriched cytoplasm in the osteocyte cell body in comparison to the parietal bone. Furthermore, quantitative tracing of the cellular processes in silico demonstrated that the numbers of the cellular processes and their bifurcation points per osteocyte in the tibia were significantly higher than those in the parietal bone. Though the total length of the processes per osteocyte in the tibia was two times longer, its total surface area and total volume were smaller than those in the parietal bone, due to its thinner diameter. These architectural differences in the osteocytes and their networks are thus implicated in the adaptation to physiologically different loading, and may also induce distinct mechanosensitivities.

© 2011 Elsevier Inc. All rights reserved.

1. Introduction

Osteocytes are embedded in the hard bone matrix of the lacunae, and form an intercellular network by extending slender cellular processes within narrow bony tubes of the canaliculi [1–4]. This structure ensures intercellular communication among bone cells including osteoblasts and osteoclasts. Osteocytes account for 90–95% of all bone cells and they are thought to sense mechanical loads and accordingly transmit the signals to osteoblasts and osteoclasts through the osteocyte network, and thus regulate bone remodeling [5–10]. Osteocytes also play a key role in phosphate metabolism by producing an endocrine factor, fibroblast growth factor 23 (FGF23), whose target organ is the kidney [11].

How osteocytes sense external loads remains unknown; however, the mechano-transduction of physical loads to the bone tissue must be tightly influenced by the structural features of bone including the lacunocanalicular and osteocyte network. Loading-induced fluid flow through the canalicular network has been thought to result in a fluid shear stress on the surface of osteocyte processes [12]. The interaction of the pericellular matrix and the osteocyte cellular process could amplify the physiological amplitude of loads to the bone tissue, thus producing sufficient levels of force to induce cellular response [13–16].

The skeletal system contains bones that are inherently loaded by distinct mechanical force patterns [17,18]. Long bones are loaded predominantly along the longitudinal direction with much higher amplitude than flat bones such as calvariae that are loaded radially and tangentially by intracranial pressure and mastication. The human fibula is estimated to have a load that is nearly twice that of the skull bone [19]. Extracellular mechanical forces are coupled to the intracellular organization of the cytoskeleton that regulates cellular connections to other cells and the extracellular matrix, thus affecting cell shape and functional outputs [20,21]. This suggests that the morphology of osteocytes, the patterning of the osteocyte network and their function are determined by external loading whose directional patterns and amplitudes are physiologically different in each bone. It is, therefore, relevant and intriguing to quantitatively manifest the structural differences of osteocytes and the osteocyte networks in distinct bones such as parietal bone and tibia.

* Corresponding authors. Address: Section of Oral Pathology, Graduate School of Medical and Dental Sciences, Tokyo Medical and Dental University, 1-5-45 Yushima, Bunkyo-ku, Tokyo 113-8549, Japan. Fax: +81 3 5803 0188.
E-mail addresses: akira.mpa@tmd.ac.jp (A. Yamaguchi), iimura.gcoe@tmd.ac.jp (T. Iimura).

This study applied three-dimensional fluorescence microscopy to fixed and decalcified bone specimens followed by surface rendering of osteocyte cell bodies and tracing of osteocyte cellular processes in silico for better imaging acquisition of the osteocyte network to compare the mouse parietal bone and tibia. These morphometric analyses revealed significant quantitative architectural differences in the osteocytes and their networks in these bones.

2. Materials and methods

2.1. Animals and preparation of skeletal tissues

Mice (laboratory strain C57BL6J) were purchased from a local distributor. The parietal bones and tibiae were dissected from 8-week-old mice after anesthetizing the animals with 0.1% ethylanthranilate. Bone specimens were fixed in 4% paraformaldehyde for 4 °C. The specimens were washed with phosphate-buffered saline, and decalcified in 20% ethylenediaminetetraaceticacid (EDTA) for 14 days for 4 °C. The decalcified specimens were embedded in an optimal cutting temperature (OCT) compound (Sakura Finetek, Tokyo, Japan) to obtain cryosections. Frontal sections of the parietal bones and longitudinal sections of tibiae (10–20 μm) were prepared, respectively. The subsequent observations were focused on the outer cortical plates of parietal bones and the diaphysis of tibiae.

2.2. Staining for actin filaments with fluorescent dye-conjugatedphalloidin

The specimens were stained with phalloidin AlexaFluor 488 (Invitrogen, Carlsbad, CA, USA) for visualizing actin-rich cell bodies and cellular processes, and BOBO-3 (Invitrogen) for counter staining of nuclear DNA with 20 μg/ml of RNAaseI (Invitrogen) at room temperature for 2 h, as previously described [22].

2.3. Confocal laser scanning images

Confocal optical sectioning was performed with a system of LSM5 Pascal5 confocal laser scanning microscopy (Carl Zeiss, Oberkochen, Germany) with a PlanFluor objective (63×, N.A. = 1.4). Two laser lines, 488 nm and 543 nm were used. The theoretical xy- and z-axes resolutions were 0.178 and 0.700 μm, respectively. The refraction index correction was 0.934. The frame size of the image was 146.2 × 146.2 μm with 512 × 512 pixels and 8-bit color depth. Pixel size was 0.286 μm. Confocal images were taken with a 0.29 μm step size for voxel sampling and then were processed four times with Kalman averaging.

2.4. Three-dimensional (3D) reconstruction followed by the morphometry of osteocytes and the cellular network tracing in silico

The 3D structure of the osteocyte network was constructed from a z-series of CLS images using IMARIS software (Bitplane, Zürich, Switzerland). The diameters of the osteocyte cell body and point-to-point distances between osteocytes were measured using the Measurement Pro function of IMARIS by rotating the 3D-reconstructed images. The surface area and volume of single osteocytes were measured by surface rendering using the Surface function of IMARIS. The threshold for the surface rendering of osteocytes was determined by super imposing the surface images to the 3D-reconstructed images until these two images overlapped. Any cellular processes measuring less than 0.5 μm in diameter were excluded in this rendering to separate the cell body and cell processes. The Filament Tracer function of IMARIS was originally developed to analyze neurite morphology and designed to recon-

struct 3D dendritic tree models. This software package was employed to obtain dendritic tree models of the osteocyte network and to quantitate the pattern of the osteocyte cellular processes by measuring the numbers of endpoints, branching points, segments between a branching point to another branching point, and the diameter, surface area and volume of each segment. The beginning point at each osteocyte was set in the 3D-reconstructed images to trace the cellular processes radiating from single osteocytes, and the endpoints of the cellular process were set in several different sizes of the diameter (0.2, 0.3, 0.4 and 0.5 μm). The average total length of the processes, the average surface area, the average volume, the average number of endpoints, the average number of branching points and the average number of segments per osteocyte were calculated by dividing each total value by the number of osteocytes analyzed.

2.5. Statistics

The mean values of the morphometric parameters were statistically analyzed using paired t-test. Differences were considered to be significant if $p < 0.01$.

3. Results

The decalcified parietal bones and tibiae of the 8-week-old mice stained by a fluorescent dye-conjugated phalloidin were scanned by the high-resolution optical slices of the confocal z-series, which clearly showed the presence of the intercellular osteocyte networks in parietal bone and tibia (Fig. 1A and B, respectively). The 3D reconstitution and the surface rendering of the osteocytes obtained from the confocal z-series images revealed the morphology of the osteocyte cell body in the parietal bone and tibia (Fig. 1C and D, respectively). The morphology of the osteocytes in the parietal bone appeared relatively spherical or oval shaped, whereas those in the tibia were elongated and spindle-shaped. This morphological distinction was quantitatively confirmed by determining the longest and shortest diameters in the 3D-reconstructed images (Table 1). The diameters of the osteocyte cell bodies in the parietal bone and tibiae ranged from 6.46 ± 0.39 to10.78 ± 0.37 μm, and from 5.71 ± 0.30 to 15.52 ± 0.92 μm, respectively. Though the shortest diameter showed no significant difference, the longest diameter of the osteocyte cell body in the tibia was 44% longer than that in the parietal bone. The ratio of the longest to the shortest diameter obviously demonstrated that the osteocytes in the tibia were more elongated than those in the parietal bones. The distances between neighboring osteocytes in the two types of bone showed no significant differences (Table 1). This study next analyzed the volume and the surface area of the osteocyte cell bodies (Table 1). The volume and the surface area of the tibial osteocytes were significantly higher than those of the parietal osteocytes. There was no significant difference in the nuclear volumes of both groups of the osteocytes (Fig. 1E and F), thus the ratios of the cellular volume was compared to the nuclear volume. This comparison demonstrated that the cytoplasmic volume in the tibial osteocytes was nearly 50% larger than that in the parietal osteocytes.

The osteocyte cellular processes were traced using the Filament Tracer function to quantitatively compare the intercellular osteocyte networks in the parietal bone and tibia. The beginning point at each single osteocyte was set in the 3D-reconstituted images, and the endpoint diameter of the cellular process was set in several different sizes (Fig. 2). Preliminary manual measurements of 3D-reconstructed images revealed the size of the cellular processes originating from the cell surface to range from approximately 0.8–0.5 μm in diameter, and that the size of recognizable slender
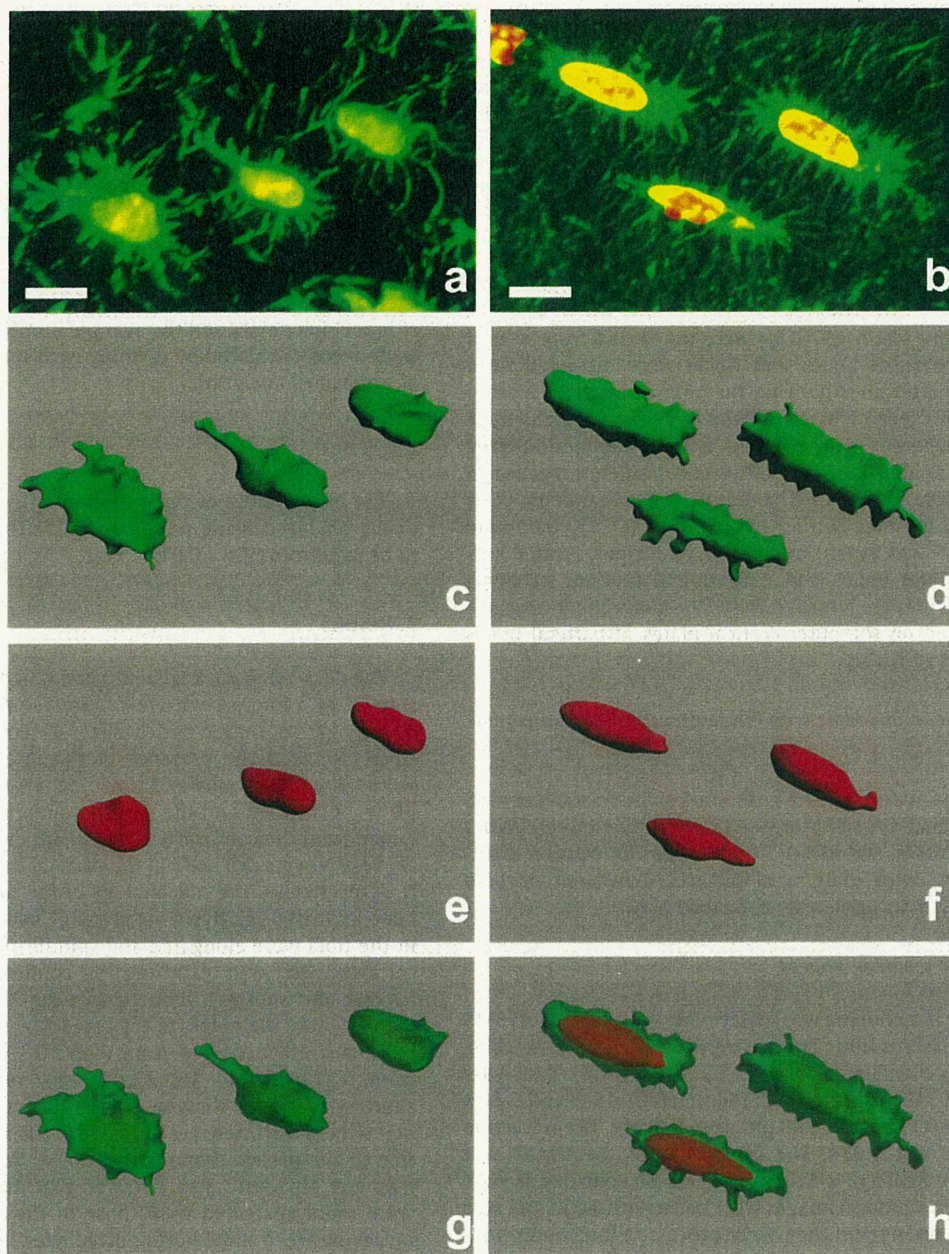
Fig. 1. Three dimensional (3D) reconstitution and surface rendering of osteocytes in the parietal bone (A, C, E and G) and tibia (B, D, F and H). The actin-rich cell body and cellular processes of osteocytes are visualized by a fluorescent dye-conjugated phalloidin (Pallioidin AlexaFluor 488) in green. Nuclei were conterstained by a cyanine nucleic acid dye (BOBO-3) in red. (A, B) Representative 3D-reconstituted images of the confocal z-series slices from parietal bone (A) and tibia (B) show osteocytes and theircellular process networks. Bar, 10 μm. (C, D) Surface renderings of osteocyte cell bodies of parietal bone (C) and tibia (D) from the 3D-reconstituted images (A and B, respectively) enable morphometric analyses (see Table 1). (E, F) Surface renderings of osteocyte nuclei of parietal bone (E) and tibia (F) from the 3D-reconstituted images (A and B, respectively) are shown. (G, H) Merged images (G and H) of the surface renderings of cell bodies and nuclei (C–E and D–F, respectively) are shown with 50% transparency of the cell bodies to visualize relative position of nucleus in cell body. (For interpretation of the references to colour in this figure legend, the reader is referred to the web version of this article.)

cellular processes forming the intercellular network and connections was nearly 0.2 μm in diameter. Therefore, the endpoints were set at 0.2, 0.3, 0.4 and 0.5 μm in diameter. Fig. 2 shows the dendritic tree models in different settings of the endpoint diameter. These tree models demonstrated that increasing number of the cellular processes and their bifurcations and more intensive and detailed appearances of the network were observed as the endpoint diameter setting got smaller in diameter. However, the settings

of 0.2 and 0.3 μm in diameter revealed that the detailed rough surfaces of the osteocyte cell bodies that did not participate in the intercellular network were traced as the cellular processes. Furthermore, quite a few of the traced networks did not fit into the recognizable osteocyte network in the 3D-reconstructed images with connecting small separated fluorescence signals. Consistently, the quantification and statistical data at these settings often showed unreasonably small values in comparison to the actual

Table 1
Morphometric data of the osteocytes in mouse parietal bone and tibia.

	Parietal bone	Tibia
Shortest diameter (μm)	6.46 ± 0.39	5.71 ± 0.30
Longest diameter (μm)	10.78 ± 0.37	15.52 ± 0.92
Diameter ratio, long/short	1.67	2.67
Cell-cell distance (μm)	22.09 ± 1.30	21.06 ± 1.20
Cell volume (μm^3)	242.93 ± 21.63	413.25 ± 41.69
Cell surface area (μm^2)	279.41 ± 24.91	458.26 ± 53.60
Nuclear volume (μm^3)	115.74 ± 7.60	135.54 ± 11.94
Volume ratio, cell/nucleus	2.1	3.05

The values are the mean ± SEM of 20 osteocytes in each bone.
* $P < 0.01$.

resolution of this microscopy system and image processing (data not shown). Therefore, the osteocyte network was further evaluated by the endpoint setting at 0.4 μm in diameter.

This *in silico* tracing of the cellular processes by Filament Tracer function was used to calculate the average length, the average volume, the average surface area and the average diameter of each segment (Table 2). All the values exhibited significant differences indicating that the tibia has a thinner cellular process network with a higher branching rate, in comparison to the parietal bone. The numbers of endpoints, branching points and segments per osteocyte in the tibia revealed higher scores than those in the parietal bones, suggesting more a comprehensive network in the tibia (Table 3). The total length of the cellular processes per osteocyte
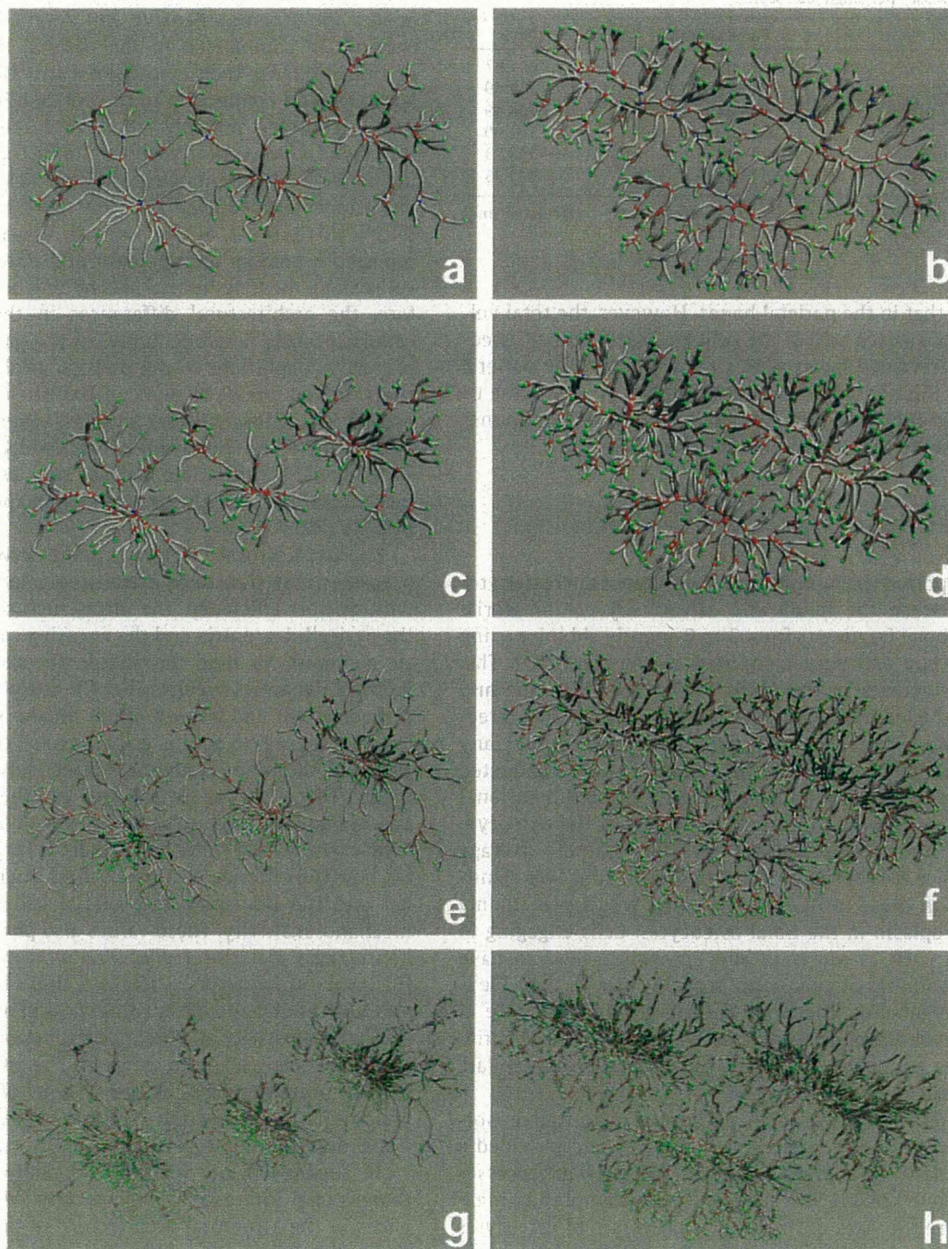

Fig. 2. Dendritic tree models of the osteocyte cellular processes in parietal bone (A, C, E and G) and tibia (B, D, F and H) from the 3D-reconstituted images (Fig. 1A and B, respectively). Dendritic tree models with different endpoint diameter settings at 0.5 μm (A and B), 0.4 μm (C and D), 0.3 μm (E and F) and 0.2 μm (G and H) are shown. Green dots, red dots and white bars indicate end points branching points and cellular process segments, respectively (see Tables 2 and 3). (For interpretation of the references to colour in this figure legend, the reader is referred to the web version of this article.)

Table 2
Morphometric values of the osteocyte networks in mouse parietal bone and tibia.

	Parietal bone	Tibia
Average length (μm)	2.57 ± 0.10	2.04 ± 0.05
Average volume (μm³)	2.39 ± 0.18	0.36 ± 0.02
Average surface area (μm²)	6.07 ± 0.35	2.26 ± 0.08
Average diameter (μm)	0.95 ± 0.05	0.39 ± 0.01

Average values per segment with the endpoint diameter setting at 0.4 μm are shown. A segment is defined as a cellular process segment from a branching point to another branching point or an endpoint. The values are the mean ± SEM.
* $P < 0.01$.

Table 3
Morphometric data of the osteocyte networks in mouse parietal bone and tibia (Total values of cellular processes per single osteocyte).

	Parietal bone	Tibia
Total length (μm)	311.06	637.67
Total volume (μm³)	288.87	112.49
Total surface area (μm²)	734.63	708.49
Total endpoints	64.00	162.00
Total branching point	58.00	152.33
Total segments	121.00	313.33

Total average values of cellular processes per single osteocyte were calculated from the values shown in Table 3.

was longer than that in the parietal bones. However, the total volume and the total surface area of the cellular processes per osteocyte in the tibia revealed lower scores than those in the parietal bone, due to the thinner diameter of the cellular process in the tibia. These findings indicated that the tibia has a longer and thinner intercellular network than that in the parietal bone.

4. Discussion

Vatsa et al. reported the morphometric differences in osteocytes and lacunae between the fibula and calvaria by combinatorial scanning of live bone fragments from 3 to 6-month-old mice using confocal microscopy and nano-computed tomography [23]. This revealed that osteocytes in the fibula had a spindle shape and stretched along the longitudinal axis of the principal loading direction, whereas those in the calvaria were spherical without any particular alignment in direction. The current study conducted two-color fluorescence morphometry by using three-dimensional confocal scanning followed by surface rendering of the osteocyte cell bodies and nuclei. This analysis revealed that the average volume and surface area of single osteocytes in the tibia was significantly larger than those in the parietal bone, which was mainly due to more cytoplasm in the tibial osteocytes. Cells engaging in active functions such as secretion and absorption tend to have relatively large volumes of cytoplasm probably due to their well-developed cell organelles. Therefore, the significant difference in the cytoplasmic volume of osteocytes between the tibia and parietal bone suggests a functional diversity in these cells to modulate bone metabolism.

A line of studies by Sugawara et al. performed quantitative morphometry for the cellular processes of osteocytes and provided a method to calculate the average length of the cellular processes per single osteocyte [24,25]. The current study attempted to measure and compare the sizes of the cellular processes of osteocytes in the parietal bone and tibia by tracing the cellular processes *in silico*. Considering the theoretical resolution of the microscopy system and the voxel size of the 3D reconstituted images, measurement of structures smaller than 0.4 μm was not expected to provide trust worthy data. In fact, the *in silico* tracings achieved

by setting the endpoint at 0.3 and 0.2 μm did not fit for the visually recognizable network of the cellular process in the 3D reconstituted images. These settings revealed artificial connections of fluorescence signals that affected reasonable measurements. Though some part of the recognizable network smaller than 0.4 μm in diameter was not entirely traced, the morphometric analysis of the cellular processes revealed significant differences in the architectures of the osteocyte networks between the parietal bone and tibia.

The analysis revealed that osteocytes in the tibia radiate a significantly larger number of the cellular processes and branches in comparison to the parietal bone. Furthermore, the surface area and volume of each segment of the cellular process in the tibia was significantly smaller than those in the parietal bone, due to its smaller diameter. These data possibly indicate that tibia developed a more comprehensive and detailed osteocyte intercellular network in comparison to the parietal bone. Mechanical forces on cells influence their cytoskeletal structure, and thus their cellular shape and connection to the surrounding cells [20,21]. Immature osteocytes possibly align themselves and develop their intercellular network in response to distinct loading patterns during bone development, when they are being embedded in osteoid. The osteocyte cell body plays a key role for initial mechano-sensing during this process, as discussed by Vatsa et al. [23]. Hirose et al. reported a gradual arrangement and flattening of cortical osteocytes along the longitudinal axis of long bone with age [26]. Therefore, the architectural differences in the osteocytes and their cellular process networks between the parietal bone and tibia are probably adaptations to the physiologically different loading patterns. In our previous work, zebrafish have a poorly developed osteocyte lacunocanalicular network, whereas amphibians, reptiles and mammals all show well-developed lacunocanalicular systems, which could be intriguing because such osteocytic adaption to the mechanical loads might be involved in the phylogenetic diversity of bone [22].

The architectural differences in the network of osteocyte cellular processes may transduce extraosseous loads to cellular responses with distinct efficiency. The ultrastructure of osteocyte processes, the pericellular matrix and the encasing canaliculi provides the basic elements for fluid flow-based theoretical models [13,15,16]. Physical dynamics predicts that the extraosseous load could cause a shear strain and a hoop strain on the surface of the processes [12,13]. These two strains are in inverse proportion to the surface area and the inner diameter, respectively, in each basic physical model. Therefore, the surface area and the diameter of the cellular process could provide critical values with the mechanosensitivity of osteocytes. On the other hand, there is little view available regarding how the other quantitative values, such as the length, the number and the branching rate of the cellular processes affect the mechanosensitivity. These values also possibly reflect the comprehensiveness of the intercellular network system rather than simply the local ultrastructure. Therefore, these factors are likely to influence the cellular and intercellular flow of molecules associated with mechanosensitivity and biological functions [27]. The current findings collectively provoke views for the architectural differences in the osteocyte networks as the systems of molecular transduction and mechanotransduction, which may be associated with the functional diversity of the osteocyte itself.

In conclusion, our quantitative analyses based on the three-dimensional fluorescence microscopy revealed significant differences in the structural architecture of the osteocyte networks in the parietal bone and tibia. These morphometric differences in the osteocyte networks between flat bone and long bone probably reflect adaptations to different physiological loading patterns to these bones, and suggest different activities of the networks. The current analysis is therefore considered to provide new insights

into the physiological, pathological and phylogenetic mechanisms of mechanosensing and metabolism in bone [28,29].

Acknowledgments

References

[1] L.F. Bonewald, Osteocyte messages from a bony tomb, Cell Metab. 5 (2007) 410–411.

[2] L.F. Bonewald, Osteocytes as dynamic multifunctional cells, Ann. NY Acad. Sci. 1116 (2007) 281–290.

[3] L.F. Bonewald, The amazing osteocyte, J. Bone Miner Res. 26 (2011) 229–238.

[4] L.F. Bonewald, M.L. Johnson, Osteocytes, mechanosensing and Wnt signaling, Bone 42 (2008) 606–615.

[5] S. Tatsumi, K. Ishii, N. Amizuka, M. Li, T. Kobayashi, K. Kohno, M. Ito, S. Takeshita, K. Ikeda, Targeted ablation of osteocytes induces osteoporosis with defective mechanotransduction, Cell Metab. 5 (2007) 464–475.

[6] S.C. Cowin, L. Moss-Salentijn, M.L. Moss, Candidates for the mechanosensory system in bone, J. Biomech. Eng. 113 (1991) 191–197.

[7] E.H. Burger, J. Klein-Nulend, Mechanotransduction in bone-role of the lacuno-canalicular network, FASEB J. 13 Suppl (1999) S101–S112.

[8] T. Nakashima, M. Hayashi, T. Fukunaga, K. Kurata, M. Oh-Hora, J.Q. Feng, L.F. Bonewald, T. Kodama, A. Wutz, E.F. Wagner, J.M. Penninger, H. Takayanagi, Evidence for osteocyte regulation of bone homeostasis through RANKL expression, Nat. Med. 17 (2011) 1231–1234.

[9] J. Xiong, M. Onal, R.L. Jilka, R.S. Weinstein, S.C. Manolagas, C.A. O'Brien, Matrix-embedded cells control osteoclast formation, Nat. Med. 17 (2011) 1235–1241.

[10] C. Lin, X. Jiang, Z. Dai, X. Guo, T. Weng, J. Wang, Y. Li, G. Feng, X. Gao, L. He, Sclerostin mediates bone response to mechanical unloading through

[11] S. Fukumoto, T.J. Martin, Bone as an endocrine organ, Trends Endocrinol. Metab. 20 (2009) 230–236.

[12] K. Piekarski, M. Munro, Transport mechanism operating between blood supply and osteocytes in long bones, Nature 269 (1977) 80–82.

[13] Y. Han, S.C. Cowin, M.B. Schaffler, S. Weinbaum, Mechanotransduction and strain amplification in osteocyte cell processes, Proc. Natl. Acad. Sci. USA 101 (2004) 16689–16694.

[14] E.J. Anderson, S. Kaliyamoorthy, J. Iwan, D. Alexander, M.L. Knothe Tate, Nano-microscale models of periosteocytic flow show differences in stresses imparted to cell body and processes, Ann. Biomed. Eng. 33 (2005) 52–62.

[15] L. You, S.C. Cowin, M.B. Schaffler, S. Weinbaum, A model for strain amplification in the actin cytoskeleton of osteocytes due to fluid drag on pericellular matrix, J. Biomech. 34 (2001) 1375–1386.

[16] L.D. You, S. Weinbaum, S.C. Cowin, M.B. Schaffler, Ultrastructure of the osteocyte process and its pericellular matrix, Anat. Rec. A Discov. Mol. Cell Evol. Biol. 278 (2004) 505–513.

[17] M. Petrtyl, J. Hert, P. Fiala, Spatial organization of the haversian bone in man, J. Biomech. 29 (1996) 161–169.

[18] R. Hillam, M. Jackson, A. Goodship, and T. Skerry, Comparison of physiological strains in the human skull and tibia, Bone 19 (1) (1996) 686–686.

[19] K.L. Lambert, The weight-bearing function of the fibula. A strain gauge study, J. Bone Joint. Surg. Am. 53 (1971) 507–513.

[20] N. Wang, J.P. Butler, D.E. Ingber, Mechanotransduction across the cell surface and through the cytoskeleton, Science 260 (1993) 1124–1127.

[21] C.S. Chen, J. Tan, J. Tien, Mechanotransduction at cell-matrix and cell-cell contacts, Annu. Rev. Biomed. Eng. 6 (2004) 275–302.

[22] L. Cao, T. Moriishi, T. Miyazaki, T. Iimura, M. Hamagaki, A. Nakane, Y. Tamamura, T. Komori, A. Yamaguchi, Comparative morphology of the osteocyte lacunocanalicular system in various vertebrates, J. Bone Miner. Metab. (2011).

[23] A. Vatsa, R.G. Breuls, C.M. Semeins, P.L. Salmon, T.H. Smit, J. Klein-Nulend, Osteocyte morphology in fibula and calvaria – is there a role for mechanosensing?, Bone 43 (2008) 452–458

[24] Y. Sugawara, R. Ando, H. Kamioka, Y. Ishihara, T. Honjo, N. Kawanabe, H. Kurosaka, T. Takano-Yamamoto, T. Yamashiro, The three-dimensional morphometry and cell-cell communication of the osteocyte network in chick and mouse embryonic calvaria, Calcif. Tissue Int. 88 (2011) 416–424.

[25] Y. Sugawara, H. Kamioka, T. Honjo, K. Tezuka, T. Takano-Yamamoto, Three-dimensional reconstruction of chick calvarial osteocytes and their cell processes using confocal microscopy, Bone 36 (2005) 877–883.

[26] S. Hirose, M. Li, T. Kojima, P.H. de Freitas, S. Ubaidus, K. Oda, C. Saito, N. Amizuka, A histological assessment on the distribution of the osteocytic lacunar canalicular system using silver staining, J. Bone Miner. Metab. 25 (2007) 374–382.

[27] T. Adachi, Y. Aonuma, K. Taira, M. Hojo, H. Kamioka, Asymmetric intercellular communication between bone cells: propagation of the calcium signaling, Biochem. Biophys. Res. Commun. 389 (2009) 495–500.

[28] T. Iimura, A. Nakane, M. Sugiyama, H. Sato, Y. Makino, T. Watanabe, Y. Takagi, R. Numano, A. Yamaguchi, A fluorescence spotlight on the clockwork development and metabolism of bone, J. Bone Miner. Metab. (2011).

[29] R.P. van Hove, P.A. Nolte, A. Vatsa, C.M. Semeins, P.L. Salmon, T.H. Smit, J. Klein-Nulend, Osteocyte morphology in human tibiae of different bone pathologies with different bone mineral density – is there a role for mechanosensing?, Bone 45 (2009) 321–329

Reduction of NOTCH1 expression pertains to maturation abnormalities of keratinocytes in squamous neoplasms

Kei Sakamoto[1], Takuma Fujii[2], Hiroshi Kawachi[3], Yoshio Miki[4], Ken Omura[5], Kei-ichi Morita[6], Kou Kayamori[7], Ken-ichi Katsube[1] and Akira Yamaguchi[1]

Notch is a transmembrane receptor functioning in the determination of cell fate. Abnormal Notch signaling promotes tumor development, showing either oncogenic or tumor suppressive activity. The uncertainty about the exact role of Notch signaling, partially, stems from inconsistencies in descriptions of Notch expression in human cancers. Here, we clarified basal-cell dominant expression of NOTCH1 in squamous epithelium. NOTCH1 was downregulated in squamous neoplasms of oral mucosa, esophagus and uterine cervix, compared with the normal basal cells, although the expression tended to be retained in cervical lesions. NOTCH1 downregulation was observed even in precancers, and there was little difference between cancers and high-grade precancerous lesions, suggesting its minor contribution to cancer-specific events such as invasion. In culture experiments, reduction of NOTCH1 expression resulted in downregulation of keratin 13 and keratin 15, and upregulation of keratin 17, and NOTCH1 knockdown cells formed a dysplastic stratified epithelium mimicking a precancerous lesion. The NOTCH1 downregulation and the concomitant alterations of those keratin expressions were confirmed in the squamous neoplasms both by immunohistochemical and cDNA microarray analyses. Our data indicate that reduction of NOTCH1 expression directs the basal cells to cease terminal differentiation and to form an immature epithelium, thereby playing a major role in the histopathogenesis of epithelial dysplasia. Furthermore, downregulation of NOTCH1 expression seems to be an inherent mechanism for switching the epithelium from a normal and mature state to an activated and immature state, suggesting its essential role in maintaining the epithelial integrity.

Notch is a transmembrane receptor that regulates cell proliferation and differentiation in various tissues. Notch is constitutively processed and is tethered on the plasma membrane as a heterodimeric protein, and the signal is transduced by the Notch intracellular domain (NICD) produced by ligand-induced cleavage,[1,2] which translocates to the nucleus and directly induces the transcription of downstream targets by forming a transactivation complex with several cofactors.[3] In humans, there are four Notch homologs (NOTCH1, 2, 3, 4) and they exhibit diverse patterns of expression, suggesting different contributions in each tissue.

The expression of Notch1, Notch2 and Notch3 in mouse skin and hair follicles has been documented,[4–7] and Notch signaling seems to have important roles in the regulation of epidermal differentiation. Conditional knockout of Notch1 in skin results in epidermal and corneal hyperplasia.[8] Overexpression of constitutively active Notch1 in basal cells leads to hyperplastic epidermis and abnormal hair development.[4,9] In contrast, deletion of Notch2, Notch3 and Notch4 does not cause significant changes in the epidermis.[6,10,11] These results indicate the significance of Notch1 in epidermal differentiation.

Abnormal Notch signaling can promote tumor development. The first indication that Notch has a role in carcinogenesis was obtained from a mouse mammary tumor virus integration assay in which four genes were identified as candidates that associate with tumor progression, the third of which (int-3) turned out to be a truncated form of Notch4.[12]

[1]Section of Oral Pathology, Tokyo Medical and Dental University, Tokyo, Japan; [2]Department of Obstetrics and Gynecology, Keio University School of Medicine, Tokyo, Japan; [3]Section of Human Pathology, Tokyo Medical and Dental University, Tokyo, Japan; [4]Section of Molecular Genetics, Medical Research Institute, Tokyo Medical and Dental University, Tokyo, Japan; [5]Section of Oral and Maxillofacial Surgery, Tokyo Medical and Dental University, Tokyo, Japan; [6]Department of Advanced Molecular Diagnosis and Maxillofacial Surgery, Hard Tissue Genome Research Center, Tokyo Medical and Dental University, Tokyo, Japan and [7]Section of Diagnostic Oral Pathology, Tokyo Medical and Dental University, Tokyo, Japan
Correspondence: Dr K Sakamoto, Section of Oral Pathology, Tokyo Medical and Dental University, Yushima 1-5-45, Tokyo 113-0034, Japan.
E-mail: s-kei.mpa@tmd.ac.jp
Received 29 August 2011; revised 25 November 2011; accepted 15 December 2011